New Global MuSyQ GPP/NPP Remote Sensing Products From 1981 to 2018

Juanmin Wang, Rui Sun, Helin Zhang, Zhiqiang Xiao, Anran Zhu, Mengjia Wang, Tao Yu, and Kunlun Xiang

***Abstract*—Long time series of vegetation productivity products are significant for the research of global carbon cycle and climate change. In this article, the 0.05° global gross primary productivity (GPP) and net primary productivity (NPP) products from 1981 to 2018 were estimated by using the improved multisource data synergized quantitative (MuSyQ) NPP algorithm. The model was based on the fraction of absorbed photosynthetically active radiation (FPAR) and leaf area index (LAI) data from the global land surface satellite (GLASS) dataset, the light use efficiency (LUE) from the parameterization approach with the clearness index (CI), the ERA-Interim meteorological data, and other environmental factors. The results suggested that the accuracy of the MuSyQ GPP product was slightly higher than that of the MOD17 GPP product when compared with the FLUXNET GPP, especially for the evergreen broadleaf forest (EBF), deciduous broadleaf forest (DBF), wetland (WET), cropland (CRO), woody savanna (WSAV), and closed shrubland (CSH) land types. MuSyQ NPP product also has higher accuracy [$R^2 = 0.81$, RMSE $= 214.6$ gC/(m^{2}year)] than MOD17 NPP [$R^2 = 0.55$, RMSE $= 214.7$ gC/(m^{2}year)] when compared with the BigFoot NPP, which indicated the reliability of the improved MuSyQ-NPP algorithm in estimating global NPP. Our results showed a significant upward trend in global NPP, which was most affected by FPAR, followed by LUE, temperature, and PAR. The average NPP declined significantly in Asia and Amazon tropical rainforests and increased significantly in Africa tropical rainforest, which were affected by the local deforestation or the forest expansion, and also the climate factors.**

***Index Terms*—Carbon cycle, GLASS, global change, vegetation productivity.**

Manuscript received October 10, 2020; revised January 21, 2021, March 26, 2021, and April 13, 2021; accepted April 21, 2021. Date of publication April 27, 2021; date of current version June 9, 2021. This work was supported in part by the National Key R&D Program of China under Grant 2017YFA0603002, and in part by the National Natural Science Foundation of China under Grant 41531174. *(Corresponding author: Rui Sun.)*

Juanmin Wang is with the State Key Laboratory of Remote Sensing Science, Beijing Engineering Research Center for Global Land Remote Sensing Products, Faculty of Geographical Science, Beijing Normal University, Beijing 100875, China, and also with the Foshan Tornado Research Center, Foshan 528000, China (e-mail: 201631170025@mail.bnu.edu.cn).

Rui Sun, Helin Zhang, Zhiqiang Xiao, Anran Zhu, Mengjia Wang, and Tao Yu are with the State Key Laboratory of Remote Sensing Science, Beijing Engineering Research Center for Global Land Remote Sensing Products, Faculty of Geographical Science, Beijing Normal University, Beijing 100875, China (e-mail: sunrui@bnu.edu.cn; 201931051035@mail.bnu.edu.cn; zhqxiao@bnu.edu.cn; 201831051047@mail.bnu.edu.cn; 201721170059@mail.bnu.edu.cn; 18953565005@189.cn, yutaogis@mail.bnu.edu.cn).

Kunlun Xiang is with the Guangdong Ecological Meteorology Center, Guangzhou 510640, China (e-mail: xiangklun@mail2.sysu.edu.cn).

Digital Object Identifier 10.1109/JSTARS.2021.3076075

I. Introduction

THE VEGETATION productivity of terrestrial ecosystems can quantify the conversion of atmospheric carbon dioxide (CO_2) to plant biomass and reflect the ability of vegetation to fix atmospheric CO_2, which is an important variable for estimating the global carbon budget, and it is also an important ecological indicator for estimating the Earth's carrying capacity and the sustainable development of terrestrial ecosystems [1]. In the early days of research on vegetation productivity, some scholars established climate productivity models based on the statistical relationship between vegetation productivity and climate factors, such as the Miami, Thomthwaite memorial [2], and Chikugo [3] approaches. Subsequently, the process-based model was established based on the eco-physiological processes of plant growth, combined with the climate and soil physical data, such as the CENTURY model [4], terrestrial ecosystem model (TEM) [5], biome bio-geochemical cycle (Biome-BGC) [6] model, and the boreal ecosystems productivity simulator (BEPS) [7]. Currently, satellite-based gross primary productivity (GPP) models have been developed based on the light use efficiency (LUE) concept [8], the LUE approach believed that photosynthetically active radiation (PAR) is the driving force for plant photosynthesis, and other external environmental factors also impact it. Most of these models' procedures use remote sensing data as some of the driving data including the Carnegie-Ames-Stanford approach (CASA) [9], the global production efficiency model (GLO-PEM) [10], the net primary productivity (NPP) algorithm of the moderate resolution imaging spectroradiometer (MODIS) (MOD17) [11]–[13], the vegetation photosynthesis model (VPM) [14], and the eddy covariance-LUE (EC-LUE) approach [15]. Many researchers have used different procedures and remote sensing data to calculate the global NPP. Nemani *et al.* [16] estimated the monthly and annual global NPP between 1982 and 1999 at 0.5° × 0.5° resolution with a biome-specific production efficiency model (PEM) using the National Center for Environmental Prediction (NCEP) climate data, the LAI and FPAR derived from the global inventory monitoring and modeling system (GIMMS), and the pathfinder advanced very high-resolution radiometer land (PAL) normalized difference vegetation index (NDVI) dataset. The results found that the average global NPP was approximately 59.7 PgC/year, with an increase of approximately 6% between 1982 and 1999. Zhao and Running [17] found that the average annual NPP decreased by 0.55% and the average was 53.5 PgC/year from 2000 to 2009 by using the 0.05° MOD17 NPP product. The new MOD17 GPP and NPP products, which span from 2000 to the present, show a temporal resolution of 8 days and a spatial resolution of 500 m [18]–[19]. Tum *et al.* [20] used the atmospheric CO_2

concentrations, the albedo map, and the climate data with the biosphere energy transfer hydrology model (BETHY/DLR) to calculate the global NPP. The result showed that the global average NPP increased by 1% from 2000 to 2014, with an average value of 60.2 PgC/year. Rafique *et al.* [21] estimated a global NPP of 63 PgC/year with a growth rate of 0.21 PgC/year from 1982 to 2012 by using the five TEMs from the trends and drivers of the regional scale sources and sinks of carbon dioxide project (TRENDY) project. The simulated NPP data were aggregated to a spatial resolution of 0.5°. These studies investigated the spatial and temporal changes in global NPP for certain periods, but most had limited temporal coverage. Longer time series and higher spatial resolution global vegetation productivity products are still required for research on global change.

Recently, the Center for Global Change Data Processing and Analysis of Beijing Normal University generated and published a long-term series of global land and terrestrial satellite (GLASS) leaf area index (LAI) and the fraction of absorbed photosynthetically active radiation (FPAR) products from 1981 to 2018 [22]–[23]. GLASS LAI and FPAR products have high accuracy, with root mean square error (RMSE) = 0.90 and bias = −0.19 for LAI [24], and RMSE = 0.08 and bias = 0.01 for FPAR [25]. Moreover, through the preprocessing of AVHRR reflectance data, including cloud contamination removal and gap filling, GLASS LAI and FPAR data are spatially complete and temporally continuous [26].

These products will be very helpful for generating the long-term series of global GPP and NPP products. At the same time, the LUE is the primary controlling factor for predicting GPP, and most LUE models used for regional or global vegetation productivity estimation only considered water stress factors and temperature stress factors. However, many studies have found that the LUE of diffuse solar radiation is higher than that of direct solar radiation [27]–[28]. The consideration of the effect of the fraction of diffuse solar radiation on LUE might improve the accuracy of GPP and NPP estimation, especially in cloudy areas, such as tropical evergreen broadleaf forests. Therefore, it is necessary to consider the influence of diffuse solar radiation when estimating the global GPP and NPP. Wang *et al.* [29] recently compared three LUE estimate approaches and found that the parameterization approach with the clearness index (CI) could improve LUE and GPP estimation. Based on the above result, this study aimed to estimate LUE by adding the CI factor to improve the accuracy of GPP estimation.

The aim of this article is as follows: (i) to propose a new global GPP and NPP products with a spatial resolution of 0.05° and a temporal resolution of 8 days from 1981 to 2018 by using the improved multisource data synergized quantitative (MuSyQ)-NPP algorithm and the GLASS LAI and FPAR products; (ii) to validate the GPP and NPP estimates based on the data of ground-based measurements from BigFoot and FLUXNET network, and (iii) to analyze the spatial-temporal distribution characteristics of global NPP.

II. Data and Methodology

A. Data

This research includes data from remote sensing imagery (e.g., LAI and FPAR), meteorology records (e.g., temperature, dewpoint temperature, surface net solar radiation, surface net thermal radiation, and surface solar radiation), digital elevation model (DEM), and land-cover information (e.g., MCD12C1 product). The specific properties of each product are shown in Table I.

TABLE I
Data Used in This Article

Data Name	Unit	Temporal resolution	Spatial resolution	Data Source
FPAR	——	8d	0.05°	GLASS
LAI	m^2/m^2	8d	0.05°	GLASS
temperature	K	12h	0.75°	ERA-Interim
dewpoint temperature	K	12h	0.75°	ERA-Interim
Surface net solar radiation	MJ/m^2	12h	0.75°	ERA-Interim
Surface net thermal radiation	MJ/m^2	12h	0.75°	ERA-Interim
Surface solar radiation downwards	MJ/m^2	12h	0.75°	ERA-Interim
Land cover product	——	1yr	0.05°	MCD12C1
DEM	km		1km	GLOBE

TABLE II
Values for Different Parameters Used in the Actual Light Use Efficiency Parameterization Depending on the Vegetation Land Cover

Vegetation type	LUE^{su}_{max} gC/MJ)	LUE^{sh}_{max} (gC/MJ)	T_{opt} (℃)
CRO	1.114	2.913	26
CSH	0.552	2.446	20
DBF	0.680	3.030	20
DNF	0.403	1.700	15
EBF	0.706	3.079	25
ENF	0.678	3.020	15
GRA	0.603	2.833	18
MF	0.795	2.917	17
OSH	0.366	1.807	16
SAV	0.615	2.914	20
WET	0.603	2.833	18
WSAV	0.562	2.810	19

1) GLASS LAI and FPAR Products: The Global Change Data Processing and Analysis Center of Beijing Normal University generated and published the GLASS product set, which includes the GLASS LAI and FPAR products. The GLASS LAI product includes two categories: the GLASS MODIS LAI product and the GLASS AVHRR LAI product. The GLASS MODIS LAI product was calculated from MODIS surface reflectance data and provided in a sinusoidal projection at a spatial resolution of 1 km and a temporal resolution of 8 days from 2000 to 2015; the GLASS AVHRR LAI product was derived from the GLASS AVHRR. The latest version of the GLASS AVHRR LAI product was provided in a geographic latitude/longitude projection at a spatial resolution of 0.05° and a temporal resolution of 8 days from 1981 to 2018 (http://www.glass.umd.edu/LAI/AVHRR/). This product was used in this study. The GLASS AVHRR FPAR product was calculated from GLASS AVHRR LAI (http://www.glass.umd.edu/FAPAR/AVHRR/) maintaining the same spatial and temporal resolution as the GLASS AVHRR LAI.

2) MODIS Land-Cover Product: The Terra and Aqua combined MODIS land-cover climate modeling grid (MCD12C1) Version 6 product has a spatial resolution of 0.05° in geographic

TABLE III
COMPARISON OF MUSYQ GPP, MOD17 GPP TO FLUXNET GPP ACCORDING TO THE DIFFERENT LAND-COVER TYPES

Land cover type	sites	8 day				Monthly				Yearly			
		MuSyQ GPP		MOD17 GPP		MuSyQ GPP		MOD17 GPP		MuSyQ GPP		MOD17 GPP	
		R^2	RMSE	R^2	RMSE	R^2	RMSE	R^2	RMSE	R^2	RMSE	R^2	RMSE
CRO	18	**0.43**	**4.39**	0.33	4.90	**0.41**	**129.28**	0.32	141.43	0.00	**561.66**	0.01	623.52
CSH	1	**0.94**	0.93	0.87	0.72	0.93	25.48	**0.95**	**14.25**				
DBF	17	**0.72**	**2.80**	0.70	3.11	**0.75**	**82.85**	0.75	90.66	0.00	580.59	0.00	**538.22**
DNF	1	0.65	1.50	**0.79**	**1.43**	0.81	52.78	0.85	38.25				
EBF	8	**0.47**	**2.61**	0.26	3.04	**0.53**	**75.38**	0.24	90.56	**0.72**	**549.45**	0.29	928.49
ENF	26	0.56	2.18	**0.64**	**1.85**	0.57	63.74	0.68	51.77	0.31	485.30	**0.41**	**394.73**
GRA	20	0.68	1.55	**0.70**	**1.51**	0.73	41.00	0.75	40.77	**0.78**	**236.57**	0.18	540.20
WET	16	**0.73**	**2.54**	0.69	3.42	**0.60**	**64.18**	0.54	68.29	**0.44**	**499.61**	0.36	532.06
WSAV	6	**0.60**	**1.74**	0.52	1.87	**0.58**	**52.85**	0.54	54.63	**0.74**	**418.86**	0.72	424.30
OSH	8	0.20	1.09	**0.34**	**1.06**	0.31	29.82	**0.37**	**31.61**	**0.05**	**225.30**	0.00	288.21
SAV	5	0.22	2.54	**0.27**	**2.45**	0.15	95.43	**0.20**	**89.84**	0.07	729.62	**0.10**	**667.09**
overall	126	**0.56**	**2.78**	0.53	2.94	**0.59**	**80.41**	0.56	84.61	**0.60**	**500.60**	0.50	549.12

TABLE IV
MEAN ANNUAL NPP OF THE WORLD'S SIX CONTINENTS, THE NORTHERN AND SOUTHERN HEMISPHERES FROM 1981 TO 2018

Region	NPP(PgC/yr)
Global	58.6
Northern Hemisphere	36.3
Southern Hemisphere	22.3
Asia	15.7
Europe	5.2
Africa	12.3
North America	8.5
South America	14.8
Oceania	2.1

TABLE V
COMPARISON OF THE DIFFERENT GLOBAL AVERAGE ANNUAL GPP ESTIMATES

Model	Time	GPP (PgC/yr)	Reference
MuSyQ	1981-2018	112.6-125.3	This paper
EC-LUE	1982-2015	112-127	Yuan et al [55]
VPM GPP V20	2000-2016	121.60-129.42	Zhang et al [54]
LUEopt	2007-2011	121.8±0.9	Madani et al [58]
CCW	2001	134.2	Zhang et al [51]
10 Land models	1990-2009	112-169	Anav et al [52]
7 LUE models	2000-2010	95.10-139.71	Cai et al [53]
BEPS	2003	132	Chen et al [48]
Flux tower observation	1982-2008	119±6	Jung et al [57]
Flux tower observation	1998-2005	123±8	Beer et al [56]
MOD17	2000-2015	110.9	Zhao et al [17]
GOSIF GPP	2000-2017	135.5 ± 8.8	Li et al [49]
GPP NIRv	1982-2018	128.3±4.0	Wang et al [50]

latitude/longitude projection and provides global land-cover types at yearly intervals, which can be downloaded from https://e4ftl01.cr.usgs.gov/MOTA/MCD12C1.006/ [30]–[31].

In this article, the IGBP product was used to address different land-cover types, which provides 17 land-cover classifications with an annual interval from 2001 to 2018. The product in 2001 was used as a substitute for the period from 1981–2000 since there was no data for before 2001 (Fig. 1).

TABLE VI
COMPARISON OF THE DIFFERENT GLOBAL AVERAGE ANNUAL NPP RESULTS

Model	Time	NPP (PgC/yr)	Reference
MuSyQ	1981-2018	55.3-61.8	This paper
ANN	1961-2010	61.46	Li et al [60]
BETHY/DLR	2000-2014	60.2	Tum et al [20]
TRENDY project	1982-2012	63	Rafique et al [61]
MME		50.6	Li et al [64]
DLEM	2000-2009	54.6	Pan et al [65]
251 estimates of terrestrial NPP		56.4	Ito,A [66]
MOD17	2000-2015	53.5	Zhao et al [17]
Ajtay, RSM		59.9,62.6	Huston et al [67]
satellite-based model	1982-1999	59.7	Nemani et al [16]
IPCC 3rd Assesment Report, fig.3.1		60	IPCC(2001) [63]
IPCC 2nd Assesment Report, fig.2.1		61.3	IPCC(1996) [62]
17 models		44.4-66.3	Cramer et al [59]
CASA	1983-1988	56-60	Potter et al [68]
CASA	1982-1990	56.4	Malmstrom et al [69]
CASA	2000-2009	50.49	Potter et al [73]
TEM		49	McGuire et al [70]
TEM		53.2	Melillo et al [71]
DEMETER		62.1	Foley [72]

3) Meteorological Data: The ERA-Interim database was used as the meteorological input data in our algorithm. It refers to a global atmospheric reanalysis data generated by the European Centre for Medium-Range Weather Forecasts (ECMWF) from 1979 to 2019 and can be downloaded from https://apps.ecmwf.int/datasets/data/interim-full-daily/levtype=sfc/ [32]. In our research, the dewpoint temperature, air temperature, surface net solar radiation, surface net thermal radiation, surface solar radiation downward, and total precipitation of 8 days were obtained by averaging the 12-h data. The relative humidity was calculated from the dewpoint temperature and average temperature [33]. A bilinear interpolation was used to produce the 0.05° data of solar radiation. However, in the interpolation of air temperature, the effect of altitude was also taken into account. The air temperature was corrected to the sea level temperature value first by the lapse rate of temperature ($\gamma = -0.65°\text{C}/100\text{ m}$). Then, a bilinear

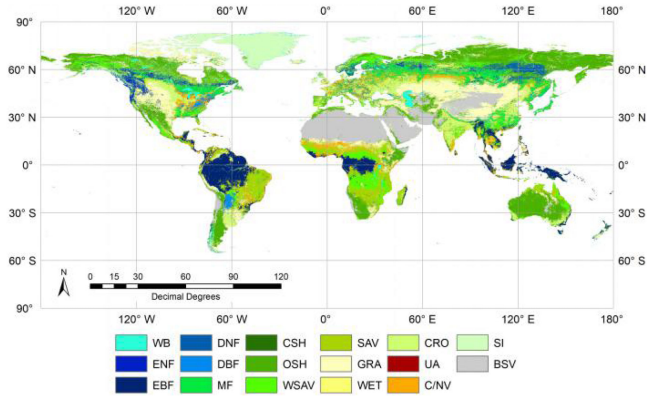

Fig. 1 Global land-cover map of the IGBP classification schemes. The full name of each land-cover type is as follows: EBF: evergreen broadleaf forest; DBF: deciduous broadleaf forest; ENF: evergreen needleleaf forest; DNF: deciduous needleleaf forest; MF: mixed forest; CSH: closed shrublands; OSH: open shrublands; WSAV: woody savannas; SAV: savannas; GRA: grasslands; WET: permanent wetlands; CRO: croplands; UA: urban area; C/NV: cropland/natural vegetation mosaic; SI: snow and ice; BSV: barren or sparsely vegetated; WB: water bodies.

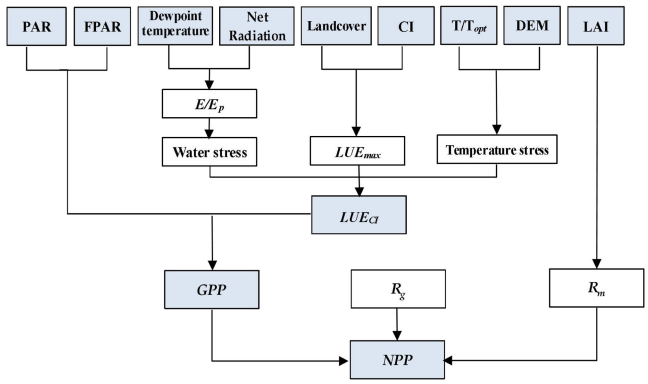

Fig. 2 Diagram of GPP and NPP estimation with the improved MuSyQ-NPP algorithm.

interpolation method was used to generate the global sea level temperature at a spatial resolution of 0.05°. Finally, the DEM data and γ were used to simulate the corrected temperature under the undulating terrain to generate global temperature data.

Zhang *et al.* [34] evaluated the solar radiation incident at the Earth's surface (Rs) estimates from six current representative global reanalyses [National Centers for Environmental Prediction-National Center for Atmospheric Research (NCEP-NCAR); National Centers for Environmental Prediction-Department of Energy (NCEP-DOE); The NCEP Climate Forecast System Reanalysis (CFSR); ERA-Interim; The Modern-Era Retrospective Analysis for Research and Applications (MERRA), and the Japan Meteorological Agency (JRA-55)] using surface measurements from different observation networks. The results showed that relatively small discrepancies were found for the ERA-Interim solar radiation product. So we selected the ERA-Interim product in our study.

4) Digital Elevation Model (DEM) Data: The DEM data were derived from the Global Land One-Kilometer Base Elevation (GLOBE) Version 1.0 (http://www.ngdc.noaa.gov/mgg/topo/globe.html) [35]. The GLOBE DEM is a global dataset covering from 180° west to 180° east longitude and 90° north to 90° south latitude; the spatial resolution of these data was 1 km.

B. Methodology

1) Model Algorithm: The MuSyQ NPP product was derived from a LUE model, which has been preliminary validated in China by Cui *et al.* [36] and at the global scale by Yu *et al.* [37]. The results suggested the proposed algorithm as potentially suitable for the estimation of the vegetation productivity. In this article, the global GPP and NPP were estimated with an improved MuSyQ-NPP algorithm (Fig. 2). The algorithm was improved in the calculation of the LUE factor.

GPP (gC/m^{2}d) was estimated according to the Monteith concept [8], which considers that GPP is proportional to the absorbed photosynthetically active radiation (APAR = FPAR × PAR) and the proportionality LUE factor as follows:

$$GPP = LUE_{CI} \times APAR \tag{1}$$

where LUE_{CI} is the actual LUE (gC/MJ), and PAR is the incident photosynthetically active radiation (MJ/m^2 d). LUE_{CI} was derived from a parameterization approach, in which the maximum LUE without stress was determined according to the vegetation type and CI, and the actual LUE was estimated by multiplying the temperature stress and water stress. The CI was adopted to take into account the effect of diffuse solar radiation on LUE. The accuracy of LUE by using this method was proved higher than the method without CI [29].

$$LUE_{CI} = \left[LUE^{su}_{\max} \times CI + LUE^{sh}_{\max} \times (1 - CI)\right] \times f(W) \times f(T). \tag{2}$$

$$CI = \frac{SW_{\text{surface}}}{SW_{\text{top}}} \tag{3}$$

$$SW_{\text{top}} = \frac{TD}{\pi} S_0 \left(\omega_0 \sin\varphi \sin\delta + \cos\varphi \cos\delta \sin\omega_0\right) \tag{4}$$

$$S_0 = \overline{S_0} \times \left(1 + 0.033 \times \cos\left(2\pi \times \frac{\text{day}}{365}\right)\right)^2. \tag{5}$$

LUE_{CI} (gC/MJ) was calculated by weighting $LUE_{\max}$ for sunlit leaves ($LUE^{su}_{\max}$, gC/MJ) and shaded leaves ($LUE^{sh}_{\max}$, gC/MJ). $LUE^{su}_{\max}$ and $LUE^{sh}_{\max}$ values for different vegetation types (Table II) were optimized by the shuffled complex evolution procedure developed at the University of Arizona (SCE-UA) [38] and FLUXNET GPP data. CI and (1 − CI) correspond to the weighted coefficients where the CI is the clearness index, which represents the ratio of solar incident radiation on the surface of the earth ($SW_{surface}$, MJ/m^{2}d) to the extraterrestrial radiation at the top of the atmosphere (SW_{top}, MJ/m^{2}d). SW_{surface} is the surface solar radiation downwards, which was obtained from the ERA-Interim dataset. *TD* represents the time period of a day ($TD = 60 \times 60 \times 24 = 86\,400$ s) and $\overline{S_0}$ is the solar radiation constant (1367 W/m^2). φ, ω_0, and δ refer to the latitude, solar horizon at sunrise, and solar declination, respectively.

f(W) describes the water stress factor and can be obtained by the following formula:

$$f(W) = 0.5 + 0.5\,(E/E_p) \tag{6}$$

where E represents the actual evapotranspiration (mm), which is calculated from a modified Penman-Monteith approach [39]–[40] using the GLASS LAI products. E_p represents the potential evapotranspiration (mm), which is derived from the Priestley and Taylor equation [41]. *f(W)* is forced to be equal to 1.0 when it exceeds 1.0.

f(T) is a temperature stress factor; the growth performance of vegetation is influenced by both the average temperature (T, °C) and the optimum growth temperature (T_{opt}, °C), which can be described as follows:

$$f(T) = \frac{1}{\left[1 + e^{0.2(T_{opt}-10-T)}\right] \times \left[1 + e^{0.3(-T_{opt}-10+T)}\right]} \quad (7)$$

where T_{opt} is the average temperature when vegetation grows best. We counted the average temperature in the month when LAI reached the maximum for different vegetation types first, and then SCE-UA optimization algorithm was used to optimize the T_{opt} value for different vegetation types (Table II).

PAR was calculated from SW_{surface} using the following formula:

$$PAR = 0.48 \times SW_{\text{surface}} \quad (8)$$

NPP (gC/m^{2}d) is the net flow of carbon entering the plants from the atmosphere and represents the remainder after deducting the organic matter consumed by plant autotrophic respiration from GPP.

$$NPP = GPP - R_a \quad (9)$$

where R_a is the autotrophic respiration (gC/m^{2}d). It can be separated into two parts, maintenance respiration R_m and growth respiration R_g, which refer to the energy necessary to maintain biomass and the energy converting assimilates into new structural plant constituents, respectively [36].

$$R_a = R_m + R_g \quad (10)$$

$$R_m = M_i r_{m,i} Q_{10,i}{}^{(T-T_b)/10} \quad (11)$$

$$R_g = \gamma(GPP - R_m) \quad (12)$$

where M_i is the live biomass of plant component i, which was calculated by using the LAI and annual maximum LAI for each pixel. $\mathrm{r_{m,i}}$ is the maintenance respiration coefficient for component i, whereas Q_{10} is the temperature sensitivity factor, T is the daily average temperature, and T_b is the base temperature. R_g was considered to be proportional to the difference between GPP and R_m. γ is the growing respiration efficient defined as 0.25.

By using the improved MuSyQ-NPP algorithm, the global GPP and NPP products with a spatial resolution of 0.05° in every 8 days from 1981 to 2018 were generated. The products can be downloaded at http://doi.org/10.5281/zenodo.3996814 [42].

2) Analyzing Method: The two methods of unary linear regression and the Pearson correlation coefficient were used to analyze the interannual change trend of NPP and the correlation between NPP and climate factors, respectively.

a) Unary Linear Regression: To understand the global NPP changes, unary linear regression was used to obtain the slope of the change in the annual NPP for each pixel by performing a linear regression on the annual average NPP for the years during the study period.

$$\theta = \frac{n \times \sum_{i=1}^{n} i \times NPP_i - \sum_{i=1}^{n} i \sum_{i=1}^{n} NPP_i}{n \times \sum_{i=1}^{n} i^2 - \left[\sum_{i=1}^{n} i\right]^2} \quad (13)$$

where θ is the slope variation in annual NPP, n represents the number of years, i represents the serial number of years, and NPP_i represents the NPP value at year i. The result (θ), which is greater than 0, represents the increase in NPP, while less than 0 represents the decrease in NPP.

b) Pearson Correlation Coefficient: The Pearson correlation method was used to calculate the correlation coefficient between the annual NPP and the annual mean air temperature and annual precipitation. The formula is shown as follows:

$$r_{xy} = \frac{\sum_{i=1}^{n} (x_i - \bar{x})(y_i - \bar{y})}{\sqrt{\sum_{i=1}^{n} (x_i - \bar{x})^2 \sum_{i=1}^{n} (y_i - \bar{y})^2}} \quad (14)$$

r_{xy} is the correlation coefficient and describes the degree of linear correlation between the two variables. n is the number of years, i is the year number, x_i is the NPP in year i, $\bar{x}$ is the average NPP, y_i is the value of the climate factor in year i, and $\bar{y}$ is the average value of the climate factor. Three confidence levels of $p < 0.01$, $p < 0.05$, and $p < 0.1$ were considered in this article.

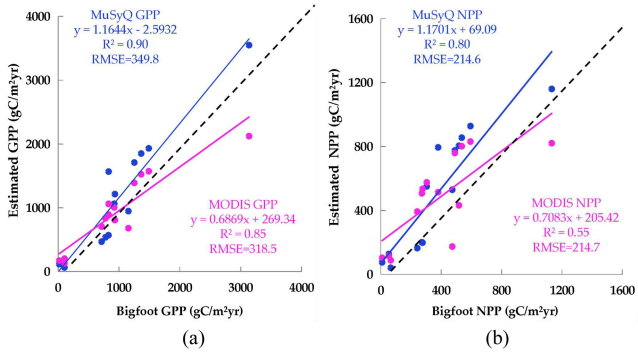

(a) (b)

Fig. 3 (a) Comparison of MuSyQ GPP, MOD17 GPP to BigFoot GPP. (b) Comparison of MuSyQ NPP, MOD17 NPP to BigFoot NPP.

III. Results

A. Validation of GPP/NPP Products

1) Validation From BigFoot GPP/NPP: In order to validate the accuracy of MuSyQ GPP and NPP products, the BigFoot GPP and NPP data for nine sites from 2000 to 2004 were downloaded (https://daac.ornl.gov/cgi-bin/dataset_lister.pl?p=1) [43]–[44], which covered a 7 × 7 km^2 area with a spatial resolution of 25 m for each site. The MOD17 product (http://files.ntsg.umt.edu/data/NTSG_Products/MOD17/) for the comparison with MuSyQ GPP and NPP was downloaded providing a temporal resolution of 8 days and spatial resolution of 0.05°. Annual data were calculated by accumulating the value of every 8 days according to the normal year or leap year.

The average values of 5 × 5 km^2 around the center pixel of BigFoot sites were calculated to correspond to the 0.05° GPP and NPP products. The results showed that the accuracy of the MuSyQ GPP product was slightly higher than that of the MOD17 GPP (Fig. 3). A higher R^2 demonstrated that the MuSyQ NPP

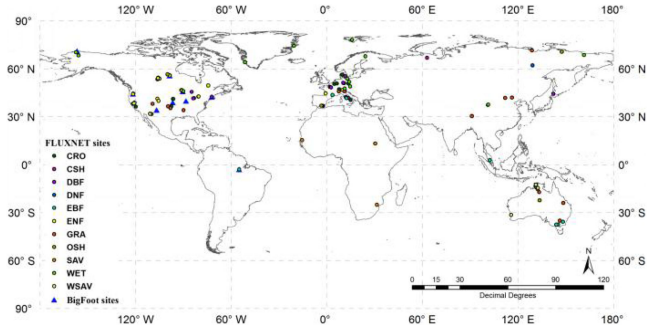

Fig. 4 Location of the selected 126 FLUXNET sites and the 9 BigFoot sites.

achieved a better precision than the MOD17 NPP product, which indicated the reliability of the improved MuSyQ-NPP algorithm in estimating global NPP.

2) Validation From FLUXNET2015 Dataset: The FLUXNET 2015 dataset [45] (https://FLUXNET.fluxdata.org/) was downloaded in order to further verify the accuracy of MuSyQ GPP data. This dataset includes observation data of the carbon flux and other climate data from 212 global FLUXNET sites. A total of 126 sites were extracted where the land-cover types matched the MCD12C1 data. These sites covered 11 land-cover types across frigid to tropical climate zones over six continents (Fig. 4).

The comparison of the MuSyQ GPP and MOD17 GPP to the FLUXNET GPP from 126 sites at 8 days, monthly and yearly scale according to different land-cover types, provides the MuSyQ GPP a higher R^2 and lower RMSE than MOD17 GPP at the three time scale (Table III). Among them, the accuracy of the MuSyQ GPP for EBF [Fig. 5(a)], DBF [Fig. 5(c)], WET [Fig. 5(e)], CRO [Fig. 5(f)], and WSAV [Fig. 5(g)] was higher than those of MOD17 GPP. The higher frequency of cloud cover in tropical rainforest reduced the values of MODIS FPAR and LAI, which resulted in the underestimation of the MOD17 GPP. In our article, GLASS FPAR and LAI were preprocessed to remove cloud contamination and fill gaps using a new time-series cloud detection algorithm [46], which resulted in a significant improvement of accuracy estimates. Direct validation result demonstrates that the GLASS LAI values were closer to the mean values of the high-resolution LAI maps (RMSE $= 0.78$ and $R^2 = 0.81$) than the MOD15 LAI values (RMSE $= 1.12$ and $R^2 = 0.67$) [26]. In particular, the estimation of MuSyQ GPP for EBF was performed better due to the increase of LUE by considering the CI factor. EBF is mainly located in tropical regions where the predominance of diffuse radiation due to more cloudy conditions with abundant rain needs to be taken into account. This is also the case of the BR-Sa1 site in the Amazon tropical rainforest. The comparative result for 8 days showed that the MOD17 GPP was severely underestimated while our GPP estimates performed better [Fig. 6(a)]. In addition, the GPP estimates for croplands were slightly higher than MOD17 GPP estimates for 8 days and monthly scales, especially for the irrigated areas in arid and semi-arid regions. This result may be explained due to the consideration of an irrigation factor in the proposed model. Such as the US-Ne1 site, our 8 days estimate was performed slightly better than MOD17 GPP in the peak values [Fig. 6(b)]. However, both MuSyQ GPP and MOD17 GPP estimates proved low accuracy at the yearly scale. For the CSH site, there is only one observation site and only one year of data, so the annual error cannot be counted. The DBF estimates in our model for 8 days and monthly scales were slightly higher than that of the MOD17 while has no advantage in yearly estimates. This conclusion was confirmed in the verification of Harvard Forest data [47]. The 8 days [Fig. 6(g)] and yearly [Fig. 6(h)] comparing result of the Harvard Forest data with the MOD17 GPP and MuSyQ GPP for DBF suggested that our estimated value was closer to the observed value in the peak period of the growing season, while both of them were higher than observed value in other time period. In terms of interannual changes, MOD17 GPP was closer to the observed value than our estimated result. Compared with the observed data, the interannual variation of estimated GPP was relatively stable for the Harvard Forest station, while the observed GPP shows an increasing trend from 1982 to 2010 and decreasing trend for 2010 to 2018. The possible reason might be that GLASS LAI and FPAR have not well reflected the effect of tree age.

At the same time, the resulting accuracy of MuSyQ GPP for ENF [Fig. 5(b)], GRA [Fig. 5(d)], and DNF [Fig. 5(h)] was lower than that of MOD17 GPP (Table III). According to the results of the RU-SkP site from DNF, the MuSyQ GPP in the growing season from 2012 to 2013 was overestimated, but it was underestimated for 2014. There is only one observation site with less observation data for DNF, which was not very representative [Fig. 6(c)]. The accuracy of MuSyQ GPP was slightly lower at 8 days and monthly scale, but higher at yearly scale than MOD17 GPP for GRA (Table III). The MOD17 GPP has a higher accuracy of ENF than our estimate, from the comparison result of the CA-obs site, there was an overestimation of the GPP during the growing season [Fig. 6(e)].

The difference between MOD17 and MuSyQ products can be mainly attributed to the difference of input data and LUE estimation. First, in MOD17 algorithm, the input remote sensing data, including FPAR and LAI, were derived from MODIS data, the PAR, and other surface meteorological fields which were provided by GEOS-5 data assimilation system at a resolution of $0.5° \times 0.67°$ in the latest version [13]. In MuSyQ model, the GLASS FPAR and LAI products were adopted, which were retrieved from NOAA AVHRR data, and the meteorological input data was derived from the ERA-Interim product at a resolution of $0.75° \times 0.75°$. Second, there are different LUE values in the MOD17 and MuSyQ model. In the MOD17 algorithm, the maximum LUE of different land-cover types can be found in the Biome parameter lookup table, and the actual LUE was calculated by multiplying temperature and VPD limits. In MuSyQ model, in order to reflect the effect of diffuse light fraction in the incident solar radiation on LUE, the maximum LUE was determined according to the vegetation type and CI, and the actual LUE was estimated by multiplying the temperature stress and water stress, where the water stress was estimated by the ratio of actual evapotranspiration and potential evapotranspiration.

B. Spatial–Temporal Characteristics of Annual NPP

1) Spatial–Temporal Patterns of Global NPP: According to the global MuSyQ NPP product, our results showed that the

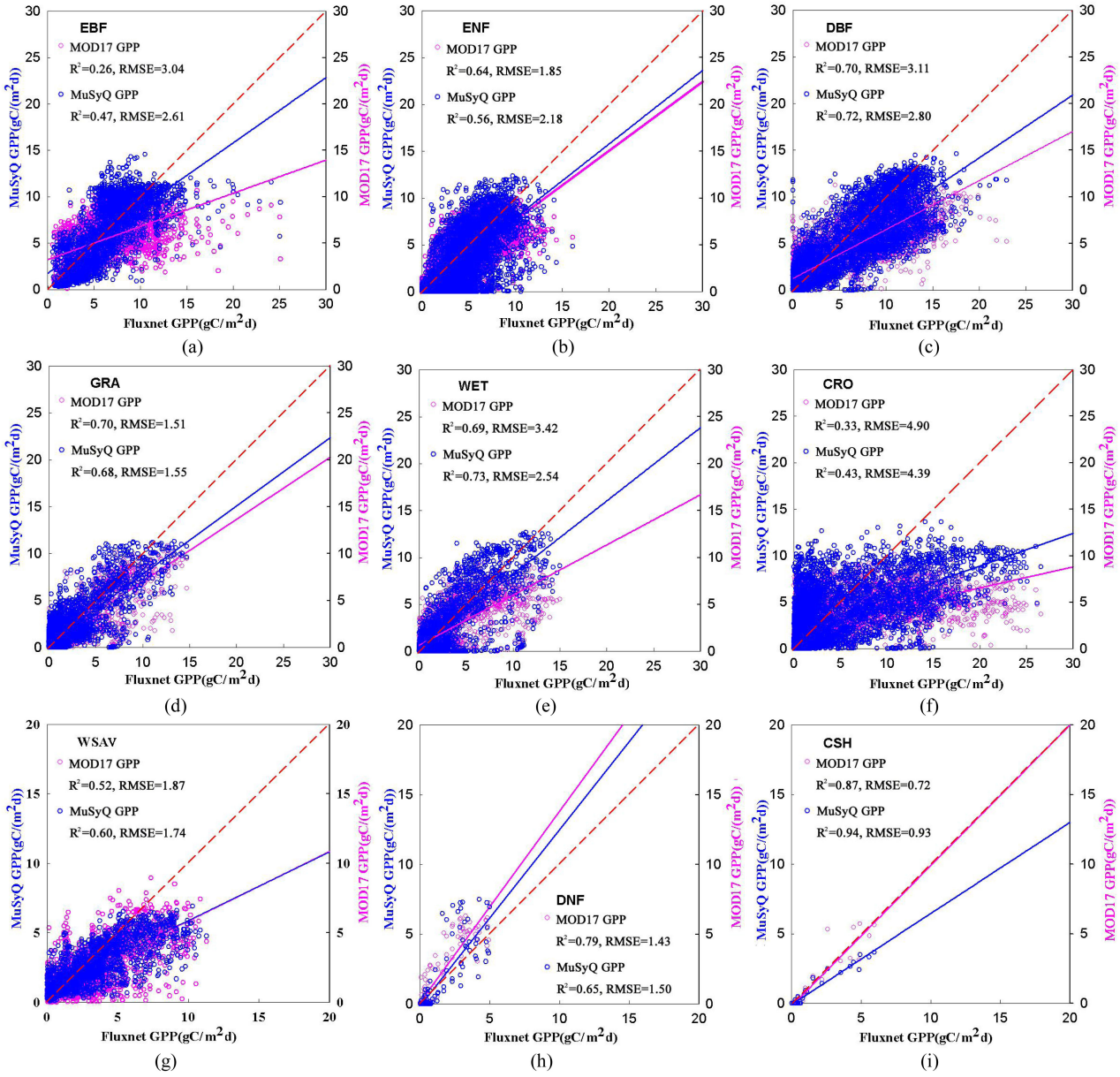

Fig. 5 Comparison of MOD17 GPP, MuSyQ GPP to FLUXNET GPP at 8 days in different land-cover types for (a) EBF; (b) ENF; (c) DBF; (d) GRA; (e) WET; (f) CRO; (g) WSAV; (h) DNF, and (i) CSH.

global annual average NPP was 58.6 PgC/year from 1981 to 2018. The spatial pattern of the global annual average NPP is shown in Fig. 7. In the tropical regions of low latitude, the temperature and humidity can fully meet the requirements of photosynthesis, the NPP value was the highest [NPP $>$ 1000 gC/(m^2 year)], while the NPP value was in the middle in the temperate regions of middle latitude [NPP $\approx$ 400–800 gC/(m^2 year)]. In the cold zone of high latitude and the other arid regions, the NPP value was the lowest [NPP $<$ 200 gC/(m^2 year)] with the main limiting factors of the temperature and precipitation. Table IV shows the average NPP of the northern and southern hemispheres and the world's six continents from 1981 to 2018. The results indicated that the NPP of the northern hemisphere was much higher than that of the southern hemisphere due to the vast land area. NPP in the northern hemisphere accounted for 61.9% of the global NPP and the southern hemisphere accounted for 38.1%. The NPP values for Asia and South America accounted for 52.1% of the global NPP, which were higher than those of the other four continents.

Fig. 8 indicates the spatial variation pattern of global annual average NPP from 1981 to 2018. The results showed that the increased regions were mainly distributed in Russia, China and India of Asia, central Europe, central and southern North America, southern South America, and central and southern Africa. The regions where NPP declines were mainly located in the northern South America and the low latitudes of Asia.

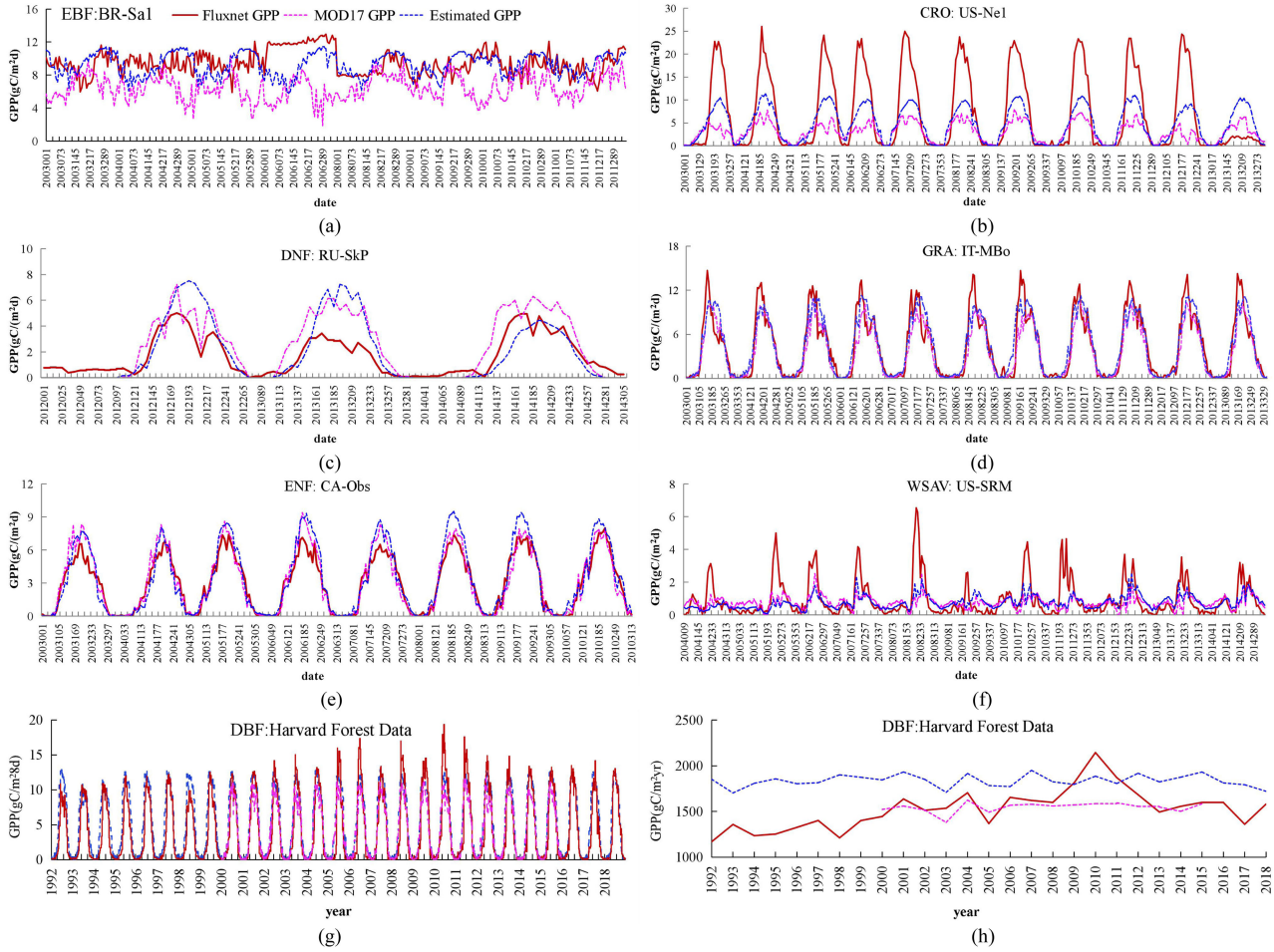

Fig. 6 Comparison of MOD17 GPP, MuSyQ GPP to FLUXNET GPP at 8 days in five FLUXNET sites for (a) EBF, (b) CRO, (c) DNF, (d) GRA, (e) ENF, and (f) WSAV. Comparison of MOD17 GPP, MuSyQ GPP to the Harvard Forest data for DBF at (g) 8 days and (h) yearly scale.

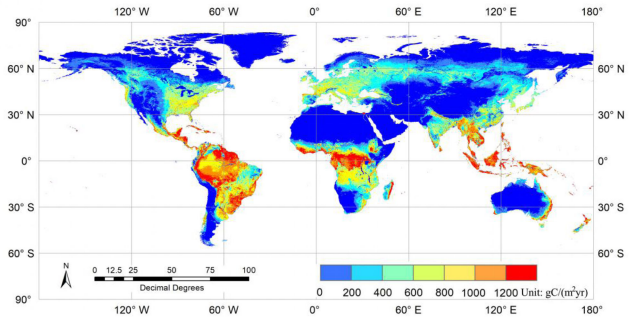

Fig. 7 Global spatial pattern of the mean annual NPP from 1981 to 2018.

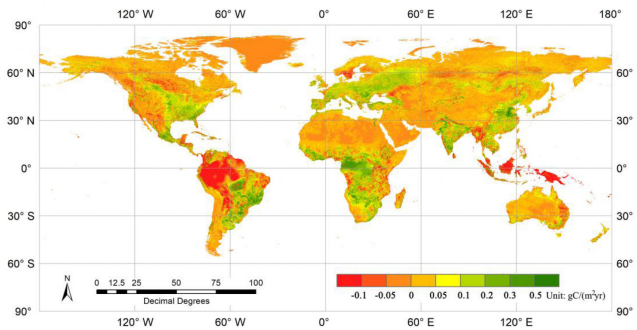

Fig. 8 Spatial variation pattern of global annual average NPP from 1981 to 2018.

The global NPP showed a significant increasing trend, with an annual upward rate of 0.10 PgC/year ($R^2 = 0.56$, $p < 0.01$) over the past 38 years [Fig. 9(a)]. The lowest was 54.8 PgC/year in 1989, and the highest was 61.1 PgC/year in 2000. Both the northern and southern hemispheres showed an upward trend. The annual growth rate was 0.09 PgC/year in the northern hemisphere and 0.01 PgC/year in the southern hemisphere. Before 2000, the curve of the global NPP was essentially consistent with that of the northern hemisphere, and after 2000, the global NPP curve was similar to the southern hemisphere [Fig. 9(b)]. In addition, the annual average NPP in Asia, Europe, Africa, North America, South America, and Oceania from 1981 to 2018 were calculated [Fig. 9(c)]. The results showed an average NPP value for Asia of 15.7 PgC/year over the 38 years, accounting for 26.8% of the world. A significant upward trend ($R^2 = 0.76$)

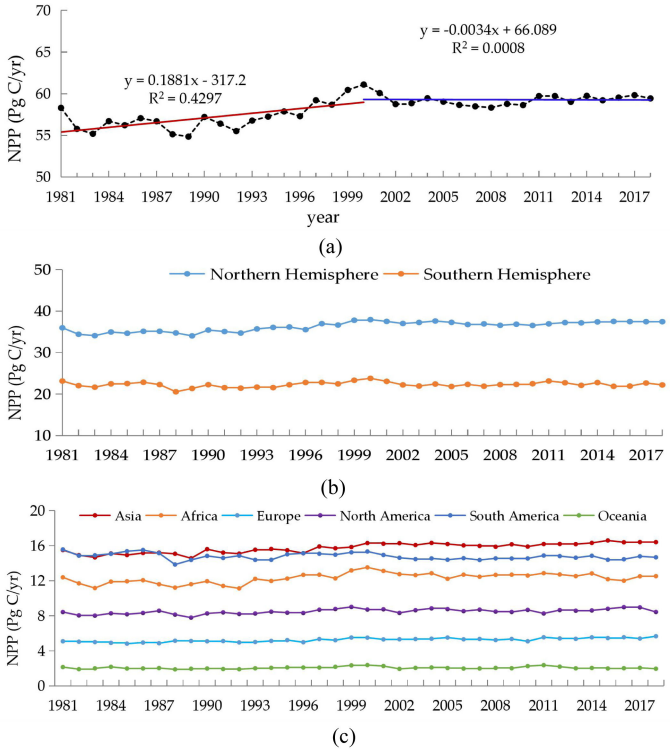

Fig. 9 Interannual NPP changes (a) at global scale; (b) for northern and southern hemisphere; (c) and for the six continents from 1981 to 2018.

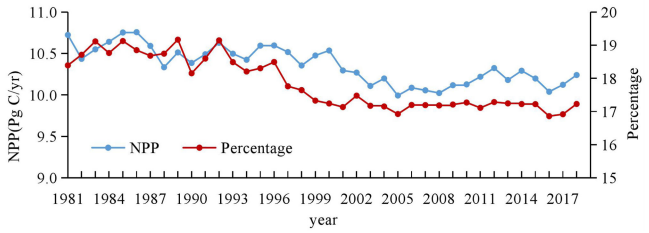

Fig. 10 Annual NPP for the three tropical rainforests and global percentages values for NPP from 1981 to 2018.

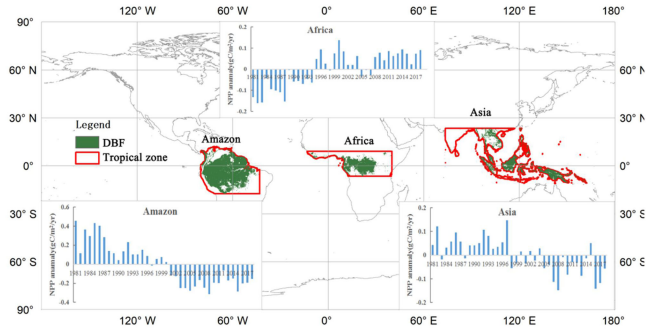

Fig. 11 NPP anomalies for EBF in the Amazon, African and Asian rainforests from 1981 to 2018.

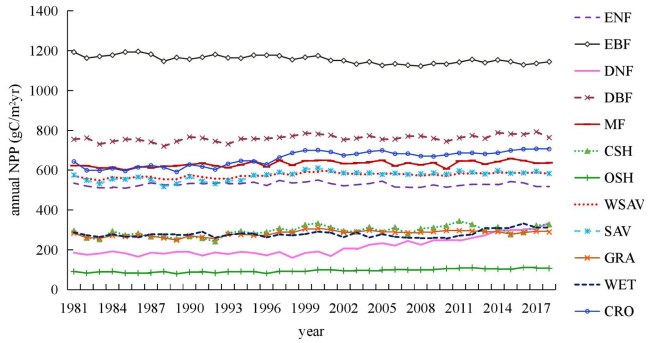

Fig. 12 Annual NPP variation for EBF, ENF, WSAV, SAV, DNF, GRA, WET, CSH, OSH, MF, CRO, and DBF from 1981 to 2018.

with an annual growth rate of 0.04 PgC/year was provided. An average NPP of 5.2 PgC/year for Europe was obtained with a significant upward trend ($R^2 = 0.67$) and an annual growth rate of 0.02 PgC/year. An average NPP value was observed 8.5 PgC/year for North America. The lowest value was 7.8 PgC/year in 1989, and the highest was 9.0 PgC/year in 1999, which indicated an upward trend and an annual growth rate of 0.02 PgC/year. An average NPP in South America of 14.8 PgC/year was found, which accounted for 25.3% of the global NPP. The lowest value was 13.9 PgC/year in 1988 and the highest was 15.6 PgC/year in 1981. This was distinct from the annual variation trend of the NPP in the other five continents, which revealed a slow downward trend. The average NPP in Africa was 12.3 PgC/year and accounted for 21.0% of the global NPP. It showed a significant upward trend before 2000, with an annual growth rate at 0.07 PgC/year. The trend was relatively stable from 2000 to 2018. The average NPP of Oceania was 2.1 PgC/year, which remained relatively stable from 1981 to 2018.

2) NPP Variation Characteristics in Tropical Rainforest: In order to further understand the changing trend of NPP in tropical rainforests, the annual NPP of the world's three largest tropical rainforests from 1981 to 2018 was calculated. The tropical regions were defined as the Amazon (17.5 °S–12 °N, 80 °W–43 °W), Africa (6.5 °S–9 °N, 13.5 °W–40 °E), and Asia (11 °S–23.5 °N, 73.5 °E–162.5 °E) in this study. Since the main vegetation types in this region are EBF, SAV, GRA, and CRO, the region of EBF in the three tropical areas was defined as tropical rainforest. The IGBP classification product of MCD12C1 from 2001 was used as the land-cover data.

The results showed that the average annual NPP of the three tropical rainforests was 10.4 PgC/year for 1981–2018. In the past 38 years, the NPP of the three tropical rainforests and their contribution to the global NPP dropped significantly (Fig. 10). Among them, the Amazon, the African, and the Asian rainforest accounted for 9.7%, 3.6%, and 4.4% of the global NPP, respectively. The Amazon rainforest NPP declined over the 38 years and almost went below the average since 2000. The NPP of the Asian rainforest was above the average before 2000 but below the average throughout the 21st century. However, the NPP of the African rainforest showed an upward trend, which was above the average from 1995 (Fig. 11).

3) NPP Variation Characteristics in Different Biomes: The annual average NPP values for different biomes from 1981 to 2018 are displayed in Fig. 12. The rank of the annual average NPP was EBF > DBF > CRO > MF > SAV > WSAV >

ENF > CSH > WET > GRA > DNF > OSH. The NPP value was highest of 1138.7 gC/(m^2year) in EBF, followed by DBF of 772.6 gC/(m^2year). The NPP of DNF, CSH, GRA, and WET were all less than 300 gC/(m^2year), and the lowest NPP was 99.6 gC/(m^2year) in OSH. The NPP interannual variation of CSH, WSAV, SAV, GRA, and CRO showed the largest increase from the late 1990s to 2000, and relatively slow after 2000. The estimated NPP values for different biomes from 2000 to 2018 were all above the 38-year average except EBF. Among them, DNF grew the fastest, with an average increase of 3.61 gC/(m^2year), followed by CRO, CSH, and SAV. The linear fitting slopes were 2.95, 1.44, and 1.40 gC/(m^2year), respectively. However, in contrast to the other biomes, EBF showed a downward tendency, and the average decline was 1.40 gC/(m^2year). EBF is mainly distributed in the tropical rainforest region, and this result was consistent with the conclusion that the decreased NPP of the Asia and Amazon tropical rainforests.

IV. Discussion

A. Comparison of Similar Research Results

1) Comparison of Global GPP and NPP Estimates From Various Models: Many studies estimated the global GPP and NPP with different methods and obtained different results. The global annual average GPP based on our model was 120.1 PgC/year, which was slightly lower than the GPP values derived from other models such as BEPS (132 PgC/year) [48], GOSIF (135.5 PgC/year) [49], NIRv (128.3 PgC/year) [50], and CCW (134.2 PgC/year) [51] and higher than the results from the MOD17 product (110.9 PgC/year) [17]. However, the value obtained by MuSyQ-NPP model was within the same range of the ten global GPP land models (112–169 PgC/year) [52] and seven LUE models (95.10–139.71 PgC/year) [53]. Moreover, it was similar to VPM V20 models outcomes (121.60–129.42 PgC/year) [54], EC-LUE model estimates (112–127 PgC/year) [55], and results from upscaling the two global flux tower observations [56]–[57] (Table V).

Global NPP estimations vary widely among different studies (Table VI), most of which range from 50.0 to 65.0 PgC/year. Our results showed that the global annual average NPP was 58.6 PgC/year, which was slightly higher than the MOD17 annual average NPP from 2001 to 2015 (53.5 PgC/year) [17]. However, the global average NPP from our results was within the result range of 17 global NPP process models (44.4–66.3 PgC/year) [59], and close to the results of Li *et al.* (61.46 PgC/year) [60], Tum *et al.* (60.2 PgC/year) [20], and Nemani *et al.* (59.7 PgC/year) [16]. This finding was consistent with the results of the IPCC second assessment (61.3 PgC/year) [62] and the IPCC Third Assessment (60 PgC/year) [63].

2) Comparison of the MuSyQ, MOD17, Revised EC-LUE, VPM, and GOSIF Products: In order to further verify the MuSyQ product, four global GPP datasets were selected which providing GPP continuous values at 0.05 × 0.05° spatial resolution with a geographic latitude/longitude projection. The revised EC-LUE GPP product was generated by using a revised LUE model [74], which includes input data of vapor pressure deficit (VPD), PAR, GLASS LAI, and atmospheric CO_2 concentration. The VPM V20 GPP product [75] was based on the improved LUE theory and driven by satellite data from MODIS and climate data from NCEP Reanalysis II. The Orbiting Carbon Observatory-2-based solar-induced chlorophyll fluorescence (GOSIF) GPP product [76] was generated by the SIF-based method and driven by the data including enhanced vegetation index (EVI) from MODIS and meteorological data (e.g., PAR, air temperature, and VPD) from the modern-era retrospective analysis for research and applications (MERRA-2).

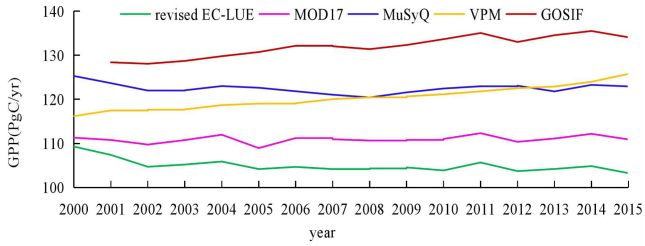

Fig. 13 Variation of global annual GPP for MuSyQ, MOD17, revised EC-LUE, VPM, and GOSIF from 2000 to 2015.

The variation of global annual GPP for MuSyQ, MOD17, revised EC-LUE, VPM, and GOSIF is shown in Fig. 13. The mean annual global GPP derived from MuSyQ was 122.5 PgC/year from 2000 to 2015. This value was similar to VPM (120.3 PgC/year), while lower than GOSIF (131.9 PgC/year) and higher than MOD17 (110.9 PgC/year) and revised EC-LUE (105.0 PgC/year). The average global annual GPP estimates of VPM and GOSIF showed a significant increasing trend, while MuSyQ, MOD17, and revised EC-LUE were almost stable during the past 16 years.

We also compared MuSyQ GPP with other GPP products in the spatial pattern. Fig. 14 was obtained by calculating the deviation of the annual average values from 2000 to 2015 between MuSyQ and the other four GPP products. In comparison with VPM, MuSyQ GPP was higher in the three major tropical rainforests of the world, and lower in southern North America, southern South America, and northern and southern Africa. MuSyQ GPP was about 400–600 gC/(m^2year) higher in the three tropical rainforests, and about 200–400 gC/(m^2 year) higher in eastern North America, Europe, and central Asia compared with MOD17. MuSyQ GPP was higher in the three major tropical rainforests, eastern North America, Europe, and central Asia, and lower in northern South America and southern Africa than the revised EC-LUE GPP. MuSyQ GPP was slightly higher in central Africa, but lower in South America, northern Africa, southern Asia, and parts of Europe than GOSIF GPP.

Combined with the global land-cover map of the IGBP classification schemes, MuSyQ GPP showed higher values than MOD17, revised EC-LUE, and VPM for EBF while closer values to GOSIF. MuSyQ, VPM, and GOSIF provided similar results in DBF and CRO estimations whereas MuSyQ GPP was relatively lower in OSH, DNF, SAV, and WSAV (Fig. 15). On the whole, MuSyQ GPP was more consistent with GOSIF estimate, while higher in the three major rainforests than the MOD17, revised EC-LUE, and VPM.

B. Reasons for NPP Interannual Changes

1) Reasons for Global NPP Interannual Changes: The global change trend of annual NPP was most affected by FPAR

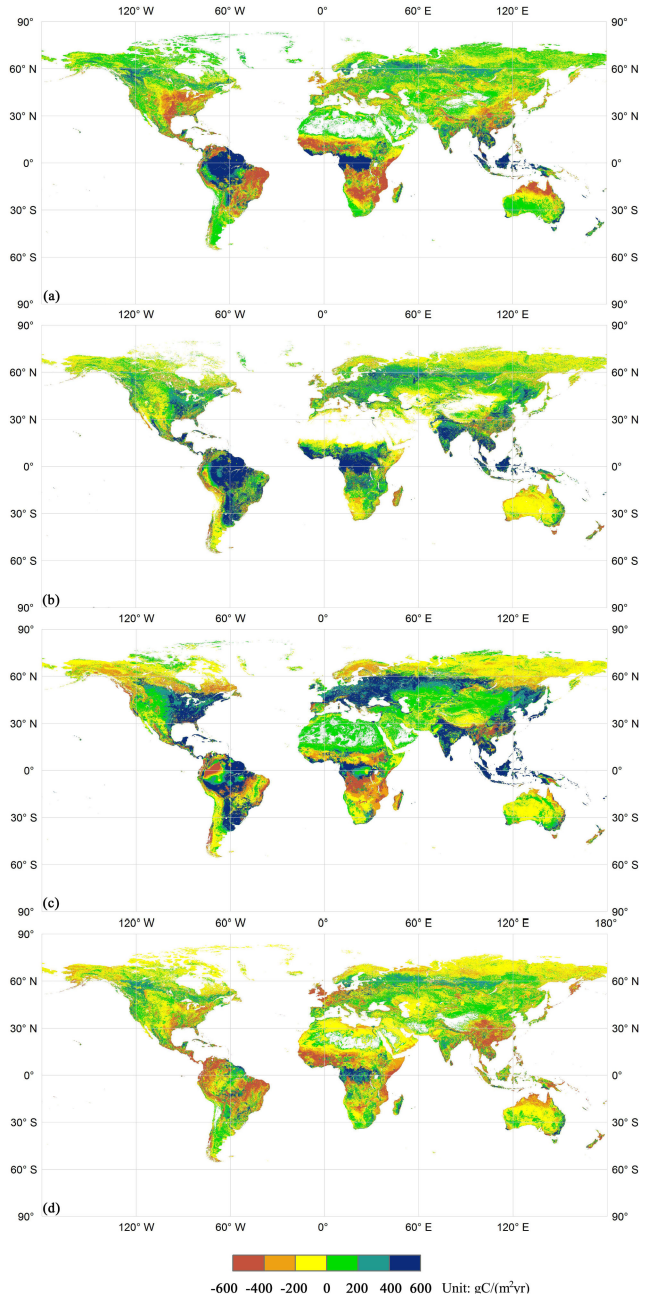

Fig. 14 Comparison of MuSyQ GPP with other GPP products. Mean annual GPP difference between MuSyQ and (a) VPM, (b) MOD17, (c) revised EC-LUE, and (d) GOSIF from 2000 to 2015. All comparisons were conducted at 0.05° × 0.05° spatial resolution.

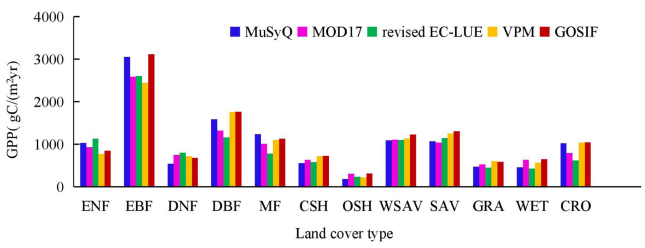

Fig. 15 Comparison of annual average MuSyQ GPP with MOD17, revised EC-LUE, GOSIF, and VPM for different land-cover types from 2000 to 2015.

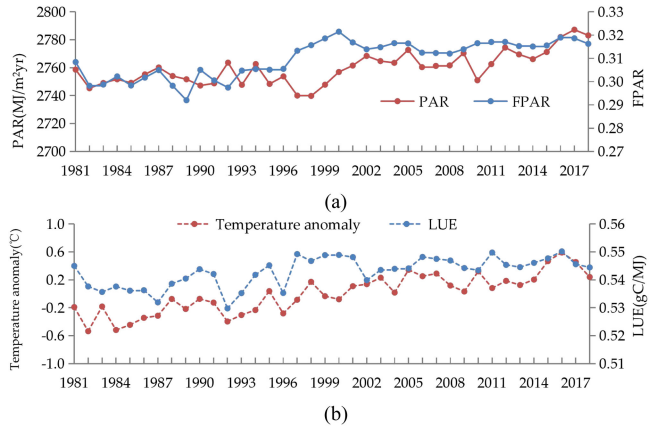

Fig. 16 (a) Global annual PAR and FAPAR. (b) Global annual LUE and temperature anomaly for 1981–2018.

(R^2 = 0.89), followed by LUE (R^2 = 0.56), temperature (R^2 = 0.35), and PAR (R^2 = 0.16) (Fig. 16). From 1981 to 2000, the global average NPP was 57.2 PgC/year, with increases of 4.89% and 2.79 PgC. The results were essentially consistent with Nemani's studies [16], which found that the global NPP rose by 6.17% and 3.42 PgC between 1982 and 1999. During this period, although the changing trend of PAR was stable, the rising trend of FPAR, LUE, and temperature was obvious, which ultimately led to an increase in GPP and NPP; at the same time, the Earth also experienced dramatic environmental changes, two of the warmest decades (the 1980s and 1990s) and three intense and persistent El Niño events happened (1982–1983, 1987–1988, and 1997–1998). The NPP declined during the three major El Niño events, with a coincident increase in global CO_2 [17]. From 2001 to 2018, the global average NPP was 59.2 PgC/year. During this period, NPP remained stable, and the overall trend of change was basically consistent with FPAR and LUE. In the meantime, NPP was also significantly affected by PAR or temperature in some years. For example, the significant increase in PAR led to an increase in NPP in 2012 and 2017, but the obviously rising temperature in 2005 resulted in a decrease in NPP. The increase of temperature strengthens the maintain respiration of vegetation, which leads to a decrease in NPP. The results also found that the NPP decreased from 2000 to 2008 and gradually recovered after 2009. Severe drought affected most of Europe, southern Africa, Brazil, and Paraguay in 2005 and much of the United States, eastern and southern Africa, China, and Australia from 2006 to 2008, which may give rise to the reduction in NPP [17]. The two volcanic eruptions in 1988 and 1993 also reduced the FPAR, which resulted in a lower NPP [25].

2) Reasons for Tropical Rainforests NPP Interannual Changes: The continued decline of Amazon and Asian rainforest NPP was related to the local deforestation. From 1982 to 2016, Brazil, Argentina, and Paraguay in South America suffered the greatest loss of forest area, and the primary forests of Australia and Southeast Asia were also deforested [77]. The Amazon drought, which began in 2005 and lasted until 2009, has led to a subsequent decline in NPP [78]. The increasing trend of Africa rainforest NPP may be attributed to the local forest expansion [77]. In addition, climatic factors such as temperature,

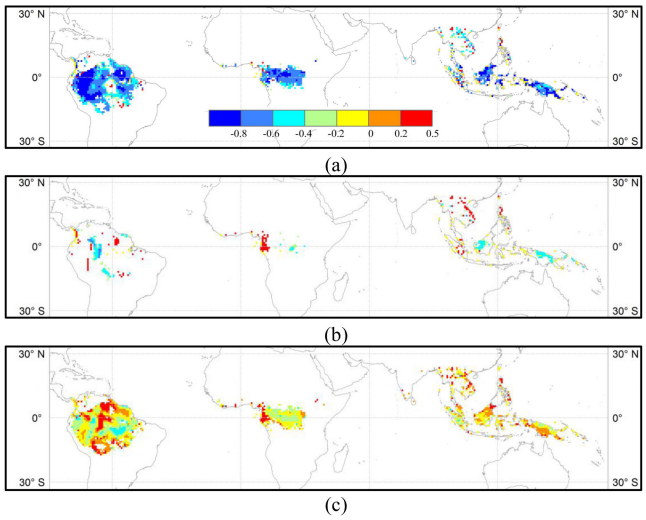

Fig. 17 (a) Spatial pattern of the correlation coefficient between the annual NPP and annual precipitation; (b) annual NPP and annual average temperature; and (c) annual NPP and annual surface solar radiation in the three tropical rainforests from 1981 to 2018.

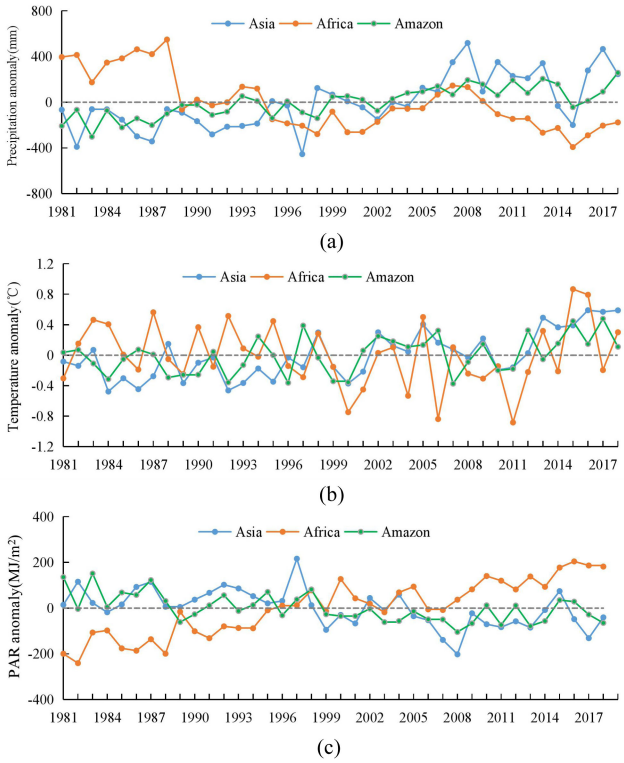

Fig. 18 (a) Annual precipitation anomaly, (b) annual temperature anomaly, and (c) annual PAR anomaly for the three tropical rainforests from 1981 to 2018.

precipitation, and solar radiation also have a certain impact on tropical rainforests NPP.

Fig. 17 displays the spatial distribution of the correlation coefficient (r) ($p < 0.05$) between the annual NPP and the climate factors from 1981 to 2018. The results showed that variations in the annual NPP over the three tropical rainforests were mainly dominated by the changes in the annual precipitation, followed by the annual surface solar radiation and the annual temperature. Among them, about 69.4% of the area showed a significant negative correlation between the NPP and the precipitation ($-1 < r < -0.6$). 29.7% of the area showed an insignificant negative correlation ($-0.6 < r < 0$), and 0.8% of the area indicated a positively correlation ($0 < r < 0.5$) [Fig. 17(a)]. According to the statistical results, the average precipitation of the Asia and Amazon tropical rainforests showed a significant increase from 1981 to 2018, with an annual increase of 14.7 mm/year ($R^2 = 0.48$) and 9.3 mm/year ($R^2 = 0.63$) [Fig. 18(a)]. The increase in precipitation would lead to less solar radiation [Fig. 18(c)], which inhibits vegetation growth. But the average precipitation of the Africa rainforests suggested a significant decrease trend, with an annual decrease of 15.9 mm/year ($R^2 = 0.52$). The decrease in precipitation meant more solar radiation [Fig. 18(c)], which lead to an increase in NPP. The temperature increased slightly in the Asia and Amazon tropical rainforests and decreased slightly in the Africa tropical rainforest [Fig. 18(b)]. The average temperature in these areas is high enough. The rising temperature will increase respiratory expenditure, which resulting in a decrease in NPP, and the decrease in temperature is conducive to the growth of vegetation. In conclusion, the slightly increased temperature, the significantly increased precipitation, and the reduced solar radiation contributed to the decrease in NPP of the Amazon and Asian rainforests. Both the decrease of precipitation and the increase of solar radiation contributed to the increase of NPP in African rainforests.

C. Uncertainty Analysis

In this article, FLUXNET GPP was used to validate the MuSyQ GPP estimates. From the scatter plot, most of the scatters (Fig. 5) were below the 1:1 line, which indicated that both our estimated GPP and MOD17 GPP were underestimated. The reason may be attributed to the large-scale difference between the *in situ* GPP observations and the 0.05° remote sensing data, and some factors that affect the LUE such as the C3 or C4 photosynthetic pathway, the concentration of CO_2 in the atmosphere, and the soil moisture were also not considered.

First, the GPP observation source area ranged from tens of meters to several kilometers, which varied with changes in instrument height, wind direction, and wind speed. At the same time, many pixels of the remote sensing data are mixed pixels. The inconsistency between the scale of the remote sensing pixel and the *in situ* GPP observation inevitably leads to uncertainty in the validation results. In our study, the correlation coefficient between the annual FLUXNET GPP and MuSyQ GPP was also calculated for the total 212 sites, which was compared to the correlation for the selected 126 sites. The result showed that the correlation of the selected 126 sites was improved [$R^2 = 0.60$, RMSE = 500.60 gC/(m^{2}year)] when compared with the total sites including mixed pixels [$R^2 = 0.47$, RMSE = 1025.06 gC/(m^{2}year)]. Even so, we cannot guarantee that the selected 126 sites are pure pixels. For example, the land-cover type of FLUXNET site BR-Sa1 (2.8567 °S, 54.9589 °W) is EBF, which

is consistent with MCD12C1 product with a spatial resolution of 5 km. Based on MCD12Q1 with a spatial resolution of 500 m, we found that the land-cover types of pixels within 5 km around the site are all EBF, and the consistency of land-cover types around the site is very high based on Google Earth images. However, at FR-Gri site (cropland site, 48.8442 °N, 1.9519 °E), although the land-cover type of the MCD12C1 pixel with a spatial resolution of 5 km is cropland, it is actually a mixed pixel. Based on MCD12Q1 with a spatial resolution of 500 m, we found that within 5 km around this site, cropland accounted for 84%, urban land accounted for 8%, and the rest were grassland or savannas. This kind of mixed pixel might cause some uncertainties and errors in the estimation. Future research should focus on the impact of inconsistent scales on validation to further verify the accuracy of the product through scale conversion by combining remote sensing data of different spatial resolutions.

Second, the C4 crops had a stronger photosynthetic capacity compared to the C3 crops. Not distinguishing between C3 and C4 crops in the LUE estimation of cropland might result in overestimation of GPP and NPP for C3 crops or underestimation of GPP and NPP for C4 crops. Future research should improve the accuracy of GPP and NPP estimates by combining more detailed land classification maps to determine the LUE of C3 and C4 crops.

Third, the CO_2 fertilization is the most important process driving the current increase in the global GPP. Ueyama *et al.* [79] found that rising CO_2 enhanced GPP at a rate of 0.08%/ppm at the global scale based on data of the 104 global eddy-covariance stations from 2000 to 2014, which was equivalent to an increase of 0.16% per year. De Kauwe *et al.* [80] found that satellite-based estimates likely underestimate the effect of CO_2 fertilization on NPP. Although the influence of CO_2 on FPAR was considered, the influence of CO_2 on LUE was not taken into account in this article. Not considering the CO_2 effect might underestimate the global GPP and NPP, especially in the later period.

In addition, soil moisture and VPD largely affect the photosynthetic rate through the control of stomatal conductance. Stocker *et al.* [81] found that the impact of soil moisture alone can reduce GPP by up to 40% at sites located in sub-humid, semi-arid, or arid regions. VPD had been used to reflect the effect of water stress on LUE in many remote sensing models, such as MOD17 [11]–[13] and the revised EC-LUE model [74]. However, under very dry conditions, VPD progressively decouples from soil moisture [81], and it cannot fully capture drought effects and explain the variability in LUE across the full dryness spectrum [82]. Stocker *et al.* [81] demonstrated that soil moisture is an important forcing of global vegetation primary production, and interannual carbon cycle variability cannot be replaced by the information of VPD and should be accounted for in satellite data-driven estimates. In our model, the ratio of actual evapotranspiration to potential evapotranspiration was used to reflect the effect of water conditions on photosynthesis, where actual evapotranspiration was calculated from a modified Penman–Monteith approach and remotely sensed LAI [36], [39]–[40]. Theoretically, actual evapotranspiration estimated from remotely sensed LAI has indirectly taken both soil moisture and VPD into account and can reflect the effect of water condition on GPP, which can partly improve the accuracy of GPP and NPP estimation, especially for irrigated cropland in semi-humid, semi-arid, and arid regions. The higher GPP and NPP estimation of croplands in this article compared with MOD17 products can partly attribute to the usage of the remotely sensed actual evapotranspiration. However, there are still errors in evapotranspiration estimation, which might bring uncertainties in the GPP and NPP estimation. Whether the ratio of actual evapotranspiration to potential evapotranspiration in this article can well reflect the effect of dry conditions globally still needed to be further studied in the future.

Finally, the land-cover map in 2001 was used as an alternative for the period from 1981 to 2000 since there was no product before 2001, which also increased the uncertainty of the estimated results.

In the future, the introduction of new remote sensing products (such as a more detailed land-cover map, soil moisture, canopy chlorophyll concentration, and solar-induced chlorophyll fluorescence) and CO_2 fertilization is expected to improve the accuracy of vegetation productivity estimates.

V. Conclusion

In this article, a new global GPP and NPP product with a spatial resolution of 0.05° and a temporal resolution of 8 days from 1981 to 2018 was generated by using the improved MuSyQ-NPP algorithm and the GLASS LAI and FPAR products. The effect of CI on LUE was added in the algorithm, which improved the estimation of GPP and NPP, especially in the tropical region. The products are spatially complete and temporally continuous owing to the characteristics of GLASS LAI and FPAR products and can be further used to estimate the global carbon budget and study the response of global vegetation on climate change and human activity.

The MuSyQ GPP and NPP were then compared with BigFoot data, FLUXNET data, and the other four GPP products. The result indicated that the accuracy of the MuSyQ GPP product was higher than that of the MOD17 GPP product when compared with the BigFoot and FLUXNET data, which suggested that the GLASS data and the MusyQ-NPP algorithm have great potential in regional and global GPP/NPP estimates.

Finally, the temporal and spatial variations in the global NPP from 1981 to 2018 were analyzed. Our results showed an average global GPP and NPP of 120.1 and 58.6 PgC/year between 1981 and 2018, respectively. The global NPP has shown a significant increasing trend, with an annual growth rate of 0.10 PgC/year over the past 38 years. The increased regions were mainly distributed in Russia, China and India in Asia, Central Europe, central and southern of North America, southern of South America, and central and southern of Africa. The NPP in the northern and southern hemispheres accounted for 61.9% and 38.1% of the global NPP, respectively. Both showed increasing trends. The NPP of the majority of land-cover types was in keeping with the general growth trend of NPP except for EBF. The average annual NPP of the three tropical rainforests from 1981 to 2018 was 10.4 PgC/year, the Asia and Amazon tropical rainforests significantly decreased, and the Africa tropical rainforest increased obviously over the 38 years; besides the reasons for local deforestation in the Asia and Amazon tropical rainforests and the forest expansion in the Africa tropical rainforest, the variations in the annual NPP were mainly affected by the changes of the precipitation, followed by PAR and temperature.

Data Availability: The 0.05° × 0.05° global GPP and NPP dataset for 1981–2018 is available at http://doi.org/10.5281/zenodo.3996814 [42]. The dataset is provided in TIFF format. The scale factor of the data is 0.01. Each TIFF file represents an 8-day GPP/NPP at a daily value (unit: gC/m^{2}d).

Appendix

TABLE VII
List of the Abbreviations and the Full Explanations in the Article

Abbreviation	Full Name
Biome-BGC	Biome Bio-Geochemical Cycle model
BEPS	Boreal Ecosystems Productivity Simulator
BETHY/DLR	The Biosphere Energy Transfer Hydrology model
BSRN	The Baseline Surface Radiation Network
BSV	Barren or sparsely vegetated.
CI	Clearness Index
CRO	Croplands
CSH	Closed Shrublands
CASA	Carnegie-Ames-Stanford Approach
CFSR	The NCEP Climate Forecast System Reanalysis
CMA	The Chinese Meteorological Administration
CO_2	Carbon Dioxide
CERES	The Earth's Radiant Energy System
DBF	Deciduous broadleaf forest
DEM	Digital Elevation Model
DNF	Deciduous Needleleaf forest
EBF	Evergreen Broadleaf Forest
EC-LUE	The Eddy Covariance-Light Use Efficiency model
ECMWF	European Centre for Medium-Range Weather Forecasts
ENF	Evergreen Needleleaf forest
EVI	Enhanced Vegetation Index
FPAR	Fraction of Absorbed Photosynthetically Active Radiation
GC-NET	The Greenland Climate Network
GEBA	The Global Energy Balance Archive
GIMMS	The Global Inventory Monitoring and Modeling System
GLASS	Global Land Surface Satellite
GLASS AVHRR	The Advanced Very High Resolution Radiometer reflectance data
GLOBE	The Global Land One-Kilometer Base Elevation
GLO-PEM	the Global Production Efficiency model
GOSAT	Greenhouse Gases Observing Satellite
GOSIF	OCO-2-based SIF product
GPP	gross primary productivity
GRA	Grasslands
IGBP	The International Geosphere-Biosphere Programme
JRA-55	The Japan Meteorological Agency
LAI	Leaf Area Index
LUE	Light Use Efficiency
MCD12C1	The combined Terra and Aqua MODIS Land Cover Climate Modeling Grid Version 6 data product
MODIS	The Moderate Resolution Imaging Spectroradiometer
MuSyQ	The improved Multisource Data Synergized Quantitative
MERRA	The Modern-Era Retrospective Analysis for Research and Applications
MF	Mixed forest
NCEP-NCAR	National Centers for Environmental Prediction-National Center for Atmospheric Research
NCEP-DOE	National Centers for Environmental Prediction-Department of Energy
NOAA	The National Oceanic and Atmospheric Administration
Nirv	New Vegetation Index
NDVI	Normalized Difference Vegetation Index
NCEI	National Centers for Environmental Information
NPP	Net Primary Productivity
OSH	Open shrublands
PAR	Photosynthetically Active Radiation
PEM	Biome-specific Production Efficiency mode
PAL	The Pathfinder Advanced Very High Resolution Radiometer Land
Rs	Incident Solar Radiation at Earth's Surface
SAV	Savannas
SCE-UA	The Shuffled Complex Evolution Procedure Developed at the University of Arizona
TEM	Terrestrial Ecosystem Model
TRENDY	Trends and drivers of the regional scale sources and sinks of carbon dioxide
UMD	The University of Maryland
VPM	Vegetation Photosynthesis Model
VPD	vapor pressure deficit
WET	Permanent wetlands
WSAV	Woody savannas

Acknowledgment

The data used in this article contain BigFoot product, FLUXNET 2015 dataset, MOD17 GPP/NPP product, revised EC-LUE product, VPM product, and GOSIF product. We sincerely thank all contributors of the data. We are also very grateful to the anonymous reviewers for their valuable suggestions on the article.

References

[1] J. M. Chen *et al.*, "Effects of foliage clumping on the estimation of global terrestrial gross primary productivity," *Global Biogeochem. Cycles*, vol. 26, no. 1, Mar. 2012, Art. no. 1019, doi: 10.1029/2010GB003996.

[2] H. Lieth, "Modeling the primary productivity of the world," in *Primary Productivity of the Biosphere. Ecological Studies (Analysis and Synthesis)*, H. Lieth and R.H. Whittaker Eds. Berlin, Heidelberg, Germany: Springer, 1975, vol. 14. pp. 203–215.

[3] Z. Uchijima and H. Seino, "Agroclimatic evaluation of net primary productivity of natural vegetations," *J. Agricultural Meteorol.*, vol. 40, no. 4, pp. 343–352, Mar. 1985, doi: 10.2480/agrmet.40.343.

[4] W. J. Parton *et al.*, "Observations and modeling of biomass and soil organic matter dynamics for the grassland biome worldwide," *Global Biogeochem. Cycles*, vol. 7, no. 4, pp. 785–809, Dec. 1993, doi: 10.1029/93GB02042.

[5] A. D. McGuire, J. M. Melillo, D. W. Kicklighter, and L. A. Joyce, "Equilibrium responses of soil carbon to climate change: Empirical and process-based estimates," *J. Biogeogr.*, vol. 22, no. 4/5, pp. 785–796, 1996a.

[6] S. W. Running, and E. Raymond Hunt, Jr., "Generalization of a forest ecosystem process model for other biomes, BIOME-BCG, and an application for global-scale models," in *Scaling Physiological Processes: Leaf to Globe*, J. R. Ehleringer and B. Christopher Eds. Field, San Diego, USA: Academic, 1993, pp. 141–158.

[7] J. Liu, J. M. Chen, J. Cihlar, and W. M. Park, "A process-based boreal ecosystem productivity simulator using remote sensing inputs," *Remote Sens. Environ.*, vol. 62, no. 2, pp. 158–175, Nov. 1997, doi: 10.1016/S0034-4257(97)00089-8.

[8] J. Monteith, "Solar radiation and productivity in tropical ecosystems," *J. Appl. Ecol.,* vol. 9, pp. 747–766, 1972, doi: 10.2307/2401901.

[9] C. S. Potter *et al.*, "Terrestrial ecosystem production: A process model based on global satellite and surface data," *Global Biogeochem. Cycles*, vol. 7, no. 4, pp. 811–841. Dec. 1993, doi: 10.1029/93GB02725.

[10] S. D. Prince, and S. N. Goward, "Global primary production: A remote sensing approach," *J. Biogeogr.*, vol. 22, pp. 815–835, 1995, doi: 10.2307/2845983.

[11] F. A. Heinsch *et al.*, "User's guide GPP and NPP (MOD17A2/A3) products NASA MODIS land algorithm," 2003. [Online]. Available: https://www.researchgate.net/publication/242118371_User's_guide_GPP_and_NPP_MOD17A2A3_products_NASA_MODIS_land_algorithm

[12] M. Zhao, F. A. Heinsch, R. R. Nemani, and S. W. Running. "Improvements of the MODIS terrestrial gross and net primary production global data set," *Remote Sens. Environ.*, vol. 95, no. 2, pp. 164–176. Mar. 2005, doi: 10.1016/j.rse.2004.12.011.

[13] S. W. Running, and M. S. Zhao, "User's guide daily GPP and annual NPP (MOD17A2/A3) products NASA earth observing system MODIS land algorithm," 2015. [Online]. Available: https://modis-land.gsfc.nasa.gov/pdf/MOD17UsersGuide2015v3.pdf

[14] X. M. Xiao *et al.*, "Satellite-based modeling of gross primary production in an evergreen needleleaf forest," *Remote Sens. Environ.*, vol. 89, no. 4, pp. 519–534. Feb. 2004, doi: 10.1016/j.rse.2003.11.008.

[15] W. P. Yuan *et al.*, "Deriving a light use efficiency model from eddy covariance flux data for predicting daily gross primary production across biomes," *Agricultural Forest Meteorol.*, vol. 143, no. 3/4, pp. 189–207. Apr. 2007, doi: 10.1016/j.agrformet.2006.12.001.

[16] R. R. Nemani *et al.*, "Climate-driven increases in global terrestrial net primary production from 1982 to 1999," *Science*, vol. 300, no. 5625, pp. 1560–1563, Jun. 2003, doi: 10.1126/science.1082750.

[17] M. S. Zhao, and S. W. Running, "Drought-induced reduction in global terrestrial net primary production from 2000 through 2009," *Science*, vol. 329, no. 5994, pp. 940–943, Aug. 2010, doi: 10.1126/science.1192666.

[18] S. Running, Q. Mu, and M. Zhao, "MOD17A2H MODIS/terra gross primary productivity 8-day L4 global 500m SIN grid V006," distributed

by NASA EOSDIS Land Processes DAAC, 2015. [Online]. Available: https://doi.org/10.5067/MODIS/MOD17A2H.006

[19] S. Running, Q. Mu, and M. Zhao, "MOD17A3H MODIS/terra net primary production yearly L4 global 500m SIN grid V006," distributed by NASA EOSDIS Land Processes DAAC, 2015. [Online]. Available: https://doi.org/10.5067/MODIS/MOD17A3H.006

[20] M. Tum, J. N. Zeidler, K. P. Günther, and T. Esch, "Global NPP and straw bioenergy trends for 2000-2014," *Biomass Bioenergy*, vol. 90, pp. 230–236. Jul. 2016, doi: 10.1016/j.biombioe.2016.03.040.

[21] R. Rafique, F. Zhao, R. De Jong, N. Zeng, and G. Asrar, "Global and regional variability and change in terrestrial ecosystems net primary production and NDVI: A model-data comparison," *Remote Sens.*, vol. 8, no. 3, pp. 1–16 Feb. 2016, doi: 10.3390/rs8030177.

[22] S. L. Liang *et al.*, "A long-term global land surface satellite (GLASS) data-set for environmental studies," *Int. J. Digit. Earth*, vol. 6, pp. 5–33. Jul. 2013, doi: 10.1080/17538947.2013.805262.

[23] S. Liang, X. Zhang, Z. Xiao, Q. Liu, J. Cheng, and X. Zhao, *Global Land Surface Satellite (GLASS) Products: Algorithms, Validation and Analysis*. Switzerland: Springer, 2013, pp. 154–155.

[24] Z. Xiao, S. Liang, and B. Jiang, "Evaluation of four long time-series global leaf area index products," *Agricultural Forest Meteorol.*, vol. 246, pp. 218–230, Nov. 2017, doi: 10.1016/j.agrformet.2017.06.016.

[25] Z. Q. Xiao, S. L. Liang, and R. Sun, "Evaluation of three long time series for global fraction of absorbed photosynthetically active radiation (FAPAR) products," *IEEE Trans. Geosci. Remote Sens.*, vol. 56, no. 9, pp. 5509–5524. Sep. 2018.

[26] Z. Xiao, S. Liang, J. Wang, Y. Xiang, X. Zhao, and J. Song, "Long-time-series global land surface satellite leaf area index product derived from MODIS and AVHRR surface reflectance," *IEEE Trans. Geosci. Remote Sens.*, vol. 54, no. 9, pp. 5301–5318, Sep. 2016.

[27] Q. C. Xin, P. Gong, A. E. Suyker, and Y. L. Si, "Effects of the partitioning of diffuse and direct solar radiation on satellite-based modeling of crop gross primary production," *Int. J. Appl. Earth Observ. Geoinf.,* vol. 50, pp. 51–63. Aug. 2016, doi: 10.1016/j.jag.2016.03.002.

[28] M. Z. He *et al.*, "Development of a two-leaf light use efficiency model for improving the calculation of terrestrial gross primary productivity," *Agricultural Forest Meteorol.*, vol. 173, pp. 28–39, May 2013, doi: 10.1016/j.agrformet.2013.01.003.

[29] M. J. Wang, R. Sun, A. R. Zhu, and Z. Q. Xiao, "Evaluation and comparison of light use efficiency and gross primary productivity using three different approaches," *Remote Sens.*, vol. 12, no. 6, May 2020, Art. no. 1003, doi: 10.3390/rs12061003.

[30] A. F. Mark, and S. M. Damien. "MCD12C1 MODIS/terra+aqua land cover type yearly L3 global 0.05Deg CMG V006 [Data set]," *NASA EOSDIS Land Processes DAAC*, 2015. [Online]. Available: https://ladsweb.modaps.eosdis.nasa.gov/missions-and- measurements/products/MCD12C1/

[31] S. M. Damien, and A. F. Mark, "User guide to collection 6 MODIS land cover (MCD12Q1 and MCD12C1) product," Version 6, May 2018. [Online]. Available: https://lpdaac.usgs.gov/documents/101/MCD12_User_Guide_V6.pdf

[32] P. Berrisford *et al.*, "The ERA-interim archive version 2.0," Version 2.0. 2011. [Online]. Available: https://www.ecmwf.int/en/elibrary/8174-era-interim-archive-version-20

[33] P. M. Zhai, "Some gross errors and biases in China's historical radiosonde data," *Acta Meteorol. Sinica*, vol. 55, no. 5, pp. 563–572. 1997, doi: 10.11676/qxxb1997.055.

[34] X. Zhang, S. Liang, G. Wang, Y. Yao, B. Jiang, and J. Cheng, "Evaluation of the reanalysis surface incident shortwave radiation products from NCEP, ECMWF, GSFC, and JMA using satellite and surface observations," *Remote Sens,* vol. 8, no. 225, pp. 1–24. Mar 2016, doi: 10.3390/rs8030225.

[35] NOAA National Geophysical Data Center, "Global land one-kilometer base elevation (GLOBE) v.1," NOAA National Centers for Environmental Information, 1999. [Online]. Available: https://doi.org/10.7289/V52R3PMS

[36] T. X. Cui *et al.*, "Estimating vegetation primary production in the Heihe river basin of China with multi-source and multi-scale data," *PLoS One*, vol. 11, no. 4, Apr. 2016, Art. no. e0153971, doi: 10.1371/journal.pone.0153971.

[37] T. Yu *et al.*, "Estimation of global vegetation productivity from global land surface satellite data," *Remote Sens.*, vol. 10, no. 2, p. 327, Feb. 2018, doi: 10.3390/rs10020327.

[38] Q. Y. Duan, S. Sorooshian, and V. Gupta, "Effective and efficient global optimization for conceptual rainfall-runoff models," *Water Resour. Res.*, vol. 28, no. 4, pp. 1015–1031, Apr. 1992, doi: 10.1029/91WR02985.

[39] C. Qiao *et al.*, "A study of shelterbelt transpiration and cropland evapotranspiration in an irrigated area in the middle reaches of the Heihe river in northwestern China," *IEEE Geosci. Remote Sens. Lett.*, vol. 12, no. 2, pp. 369–373. Feb. 2015.

[40] K. Zhang, J. S. Kimball, Q. Mu, L. A. Jones, S. J. Goetz, and S. W. Running, "Satellite based analysis of northern ET trends and associated changes in the regional water balance from 1983 to 2005," *J. Hydrol.*, vol. 379, no. 1/2, pp. 92–110, Dec. 2009, doi: 10.1016/j.jhydrol.2009.09.047.

[41] C. H. Priestley, and R. Taylor, "On the assessment of surface heat flux and evaporation using large-scale parameters," *Monthly Weather Rev.*, vol. 100, pp. 81–92, 1972, doi: 10.1175/1520-0493(1972)100<0081:OTAOSH>2.3.CO;2.

[42] R. Sun, Z. Q. Xiao, J. M. Wang, A. R. Zhu, M. J. Wang, and Q. Li, "Global vegetation productivity from 1981 to 2018 estimated from remote sensing data (Version 1.0) [Data set]," *IEEE J-STARS, Zenodo*, 2020. [Online]. Available: https://zenodo.org/record/3996814#.YKIWMlpSGUk

[43] D. P. Turner, W. D. Ritts, and M. Gregory, "BigFoot GPP surfaces for North and South American sites, 2000–2004. Data set," 2006. [Online]. Available: http://daac.ornl.gov, from Oak Ridge National Laboratory Distributed Active Archive Center, Oak Ridge, Tennessee, USA, doi: 10.3334/ORNLDAAC/749.

[44] D. P. Turner, W. D. Ritts. M, Gregory, "BigFoot NPP surfaces for North and South American sites, 2000–2004. Data set," 2006. [Online]. Available: http://daac.ornl.gov, from Oak Ridge National Laboratory Distributed Active Archive Center, Oak Ridge, Tennessee, USA, doi: 10.3334/ORNLDAAC/750.

[45] G. Pastorello *et al.*, "The FLUXNET2015 dataset and the ONEFlux processing pipeline for eddy covariance data," *Sci. Data*, vol. 7, no. 1, Jul. 2020, Art. no. 225, doi: 10.1038/s41597-020-0534-3.

[46] H. R. Tang, K. Yu, O. Hagolle, K. Jiang, X. R. Geng, and Y. C. Zhao, "A cloud detection method based on a time series of MODIS surface reflectance images," *Int. J. Digit. Earth,* vol. 6, pp. 157–171, Dec. 2013, doi: 10.1080/17538947.2013.833313.

[47] W. Munger, and S. Wofsy, "Canopy-Atmosphere Exchange of Carbon, Water and Energy at Harvard Forest EMS Tower since 1991, Harvard Forest Data Archive: HF004," 2020 [Online]. Available: https://harvardforest1.fas.harvard.edu/exist/apps/datasets/showData.html?id=HF004

[48] J. M. Chen *et al.*, "Effects of foliage clumping on the estimation of global terrestrial gross primary productivity," *Global Biogeochem. Cycles,* vol. 26, no. 1, Mar. 2012, Art. no. GB1019, doi: 10.1029/2010GB003996.

[49] X. Li, and J. F. Xiao, "Mapping photosynthesis solely from solar-induced chlorophyll fluorescence: A global, fine-resolution dataset of gross primary production derived from OCO-2," *Remote Sens.*, vol. 11, no. 21, Oct. 2019, Art. no. 2563, doi: 10.3390/rs11212563.

[50] S. Wang *et al.*, "Tracking the seasonal and inter-annual variations of global gross primary production during last four decades using satellite near-infrared reflectance data," *Sci. Total Environ.*, vol. 755, no. Pt 2, Feb. 2021, Art. no. 142569, doi: 10.1016/j.scitotenv.2020.142569.

[51] Y. L. Zhang *et al.*, "Development of a coupled carbon and water model for estimating global gross primary productivity and evapotranspiration based on eddy flux and remote sensing data," *Agricultural Forest Meteorol.,* vol. 223, pp. 116–131. Apr. 2016, doi: 10.1016/j.agrformet.2016.04.003.

[52] A. Anav *et al.*, "Spatiotemporal patterns of terrestrial gross primary production: A review," *Rev. Geophys.*, vol. 53, no. 3, pp. 785–818, Jun. 2015, doi: 10.1002/2015RG000483.

[53] W. B. Cai *et al.*, "Large differences in terrestrial vegetation production derived from satellite-based light use efficiency models," *Remote Sens.*, vol. 6, no. 9, pp. 8945–8965, Sep. 2014, doi: 10.3390/rs6098945.

[54] Y. Zhang *et al.*, "A global moderate resolution dataset of gross primary production of vegetation for 2000–2016," *Sci. Data*, vol. 4, Oct. 2017, Art. no. 170165, doi: 10.1038/sdata.2017.165.

[55] W. P. Yuan, Y. Zheng, and S. L. Piao, "Increased atmospheric vapor pressure deficit reduces global vegetation growth," *Sci. Adv.*, vol. 5, no. 8, Aug. 2019, Art. no. 1396, doi: 10.1126/sciadv.aax1396.

[56] C. Beer *et al.*, "Terrestrial gross carbon dioxide uptake: Global distribution and covariation with climate," *Science*, vol. 329, no. 5993, pp. 834–838. Aug. 2010, doi: 10.1126/science.1184984.

[57] M. Jung *et al.*, "Global patterns of land atmosphere fluxes of carbon dioxide, latent heat, and sensible heat derived from eddy covariance, satellite, and meteorological observations," *J. Geophys. Res.*, vol. 116, no. G3, Sep. 2011, Art. no. G00J07, doi: 10.1029/2010JG001566.

[58] N. Madani, J. S. Kimball, and S. W. Running, "Improving global gross primary productivity estimates by computing optimum light use efficiencies

using flux tower data," *J. Geophys. Res. Biogeoscience*, vol. 122, no. 11, pp. 2939–2951. Nov. 2017, doi: 10.1002/2017JG004142.
[59] W. Cramer *et al.*, "Comparing global models of terrestrial net primary productivity (NPP): Overview and key results," *Global Change Biol.*, vol. 5, no. S1, pp. 1–15. Apr. 1999, doi: 10.1046/j.1365-2486.1999.00009.x.
[60] P. Li *et al.*, "Quantification of the response of global terrestrial net primary production to multifactor global change," *Ecol. Indicators*, vol. 76, pp. 245–255, May 2017, doi: 10.1016/j.ecolind.2017.01.021.
[61] R. Rafique, F. Zhao, R. De Jong, N. Zeng, and G. Asrar, "Global and regional variability and change in terrestrial ecosystems net primary production and NDVI: A model-data comparison," *Remote Sens.*, vol. 8, no. 3, p. 177, Feb. 2016, doi: 10.3390/rs8030177.
[62] J. T. Houghton, L. G. Meira Filho, B. A. Callander, N. Harris, A. Kattenberg, and K. Maskell, *Climate Change 1995: The Science of Climate Change: Contribution of Working Group I to the Second Assessment Report of the Intergovernmental Panel On Climate Change*. Cambridge, U.K.: Cambridge Univ. Press, 1996.
[63] J. T. Houghton *et al.*, *Climate Change 2001: The Scientific Basis. Contribution of Working Group I to the Third Assessment Report of the Intergovernmental Panel On Climate Change*. Cambridge, U.K.: Cambridge Univ. Press, 2001.
[64] S. Li *et al.*, "The change of global terrestrial ecosystem net primary productivity (NPP) and its response to climate change in CMIP5," *Theor. Appl. Climatol.*, vol. 121, pp. 319–335. Aug. 2014, doi: 0.1007/s00704-014-1242-8.
[65] S. F. Pan *et al.*, "Complex spatiotemporal responses of global terrestrial primary production to climate change and increasing atmospheric cO_2 in the 21st century," *PLoS One,* vol. 9, no. 11, Nov. 2014, Art. no. e112810, doi: 10.1371/journal.pone.0112810.
[66] A. Ito, "A historical meta-analysis of global terrestrial net primary productivity: Are estimates converging?," *Global Change Biol,* vol. 17, no. 10, pp. 3161–3175, May 2011, doi: 10.1111/j.1365-2486.2011.02450.x.
[67] M. A. Huston, and S. Wolverton, "The global distribution of net primary production: Resolving the paradox," *Ecol. Monographs*, vol. 79, no. 3, pp. 343–377, Aug. 2009, doi: 10.1890/08-0588.1.
[68] C. S. Potter, S. Klooster, and V. Brooks, "Interannual variability in terrestrial net primary production: Exploration of trends and controls on regional to global scales," *Ecosystems*, vol. 2, pp. 36–48. Jan. 1999, doi: 10.1007/s100219900056.
[69] C. M. Malmström *et al.*, "Interannual variation in global-scale net primary production: Testing model estimates," *Global Biogeochem. Cycles*, vol. 11, no. 3, pp. 367–392, Sep. 1997, doi: 10.1029/97GB01419.
[70] A. D. McGuire *et al.*, "Equilibrium responses of global net primary production and carbon storage to doubled atmospheric carbon dioxide: Sensitivity to changes in vegetation nitrogen concentration," *Global Biogeochem. Cycles*, vol. 11, no. 2, pp. 173–189, Jun. 1997, doi: 10.1029/97GB00059.
[71] J. M. Melillo, A. D. McGuire, D. W. Kicklighter, B. Moore, C. J. Vorosmarty, and A. L. Schloss, "Global climate change and terrestrial net primary production," *Nature*, vol. 363, pp. 234–240, May 1993, doi: 10.1038/363234a0.
[72] J. A. Foley, "Net primary productivity in the terrestrial biosphere: The application of a global model," *J. Geophys. Res.*, vol. 99, no. D10, pp. 20773–20783. Oct. 1994, doi: 10.1029/94JD01832.
[73] C. Potter, S. Klooster, and V. Genovese, "Net primary production of terrestrial ecosystems from 2000 to 2009," *Climatic Change*, vol. 115, pp. 365–378, Apr.–Nov. 2012, doi: 10.1007/s10584-012-0460-2.
[74] Y. Zheng *et al.*, "Improved estimate of global gross primary production for reproducing its long-term variation, 1982–2017," *Earth Syst. Sci. Data*, vol. 12, no. 4, pp. 2725–2746, Sep. 2020, doi:10.5194/essd-12-2725-2020.
[75] Y. Zhang *et al.*, "A global moderate resolution dataset of gross primary production of vegetation for 2000–2016," *Sci. Data*, vol. 4, no. 1, Oct. 2017, Art. no. 170165, doi: 10.1038/sdata.2017.165.
[76] X. Li, and J. F. Xiao, "Mapping photosynthesis solely from solar-induced chlorophyll fluorescence: A global, fine-resolution dataset of gross primary production derived from OCO-2," *Remote Sens.*, vol. 11, no. 21, Oct. 2019, Art. no. 2563, doi: 10.3390/rs11212563.
[77] X. Song *et al.*, "Global land change from 1982 to 2016," *Nature*, vol. 560, pp. 639–643, Aug. 2018, doi: 10.1038/s41586-018-0411-9.
[78] L. L. Simon, M. B. Paulo, L. P. Oliver, M. F. V. Geertje, and N. Daniel, "The 2010 amazon drought," *Science*, vol. 331, no. 6017, p. 554. Feb. 2011, doi: 10.1126/science.1200807.
[79] M. Ueyama *et al.*, "Inferring CO_2 fertilization effect based on global monitoring land-atmosphere exchange with a theoretical model," *Environ. Res. Lett.*, vol. 15, p. 084009. Jul. 2020, doi: 10.1088/1748-9326/ab79e5.
[80] M. G. De Kauwe, T. F. Keenan, B. E. Medlyn, I. C. Prentice, and C. Terrer, "Satellite based estimates underestimate the effect of cO_2 fertilization on net primary productivity," *Nat. Climate Change*, vol. 6, no. 10, pp. 892–893, Sep. 2016, doi: 10.1038/nclimate3105.
[81] B. D. Stocker, J. Zscheischler, T. Keenan, I. Prentice, J. Penuelas, and S. Seneviratne, "Quantifying soil moisture impacts on light use efficiency across biomes," *New Phytologist*, vol. 218, no. 4, pp. 1430–1449, Mar. 2018, doi: 10.1111/nph.15123.
[82] B. D. Stocker, J. Zscheischler, T. F. Keenan, I. C. Prentice, S. I. Seneviratne, and J. Peñuelas, "Drought impacts on terrestrial primary production underestimated by satellite monitoring," *Nat. Geosci.*, vol. 12, no. 4, pp. 264–270. Mar. 2019, doi: 10.1038/s41561-019-0318-6.

Juanmin Wang was born in Shanxi Province in 1983. She is currently working toward the Ph.D. degree in geographic information system at Beijing Normal University, Beijing, China.

From 2007 to 2018, she was with the Meteorological Bureau of Shaanxi Province, and since 2019, she has been with the Meteorological Bureau of Foshan City. Her research interests include the remote sensing applications on ecological environment.

Rui Sun received the B.S. degree in agrometeorology from the Nanjing Institute of Meteorology, Nanjing, China, in 1992, the M.S. degree in applied meteorology from Graduate School, Chinese Academy of Agriculture Sciences, Beijing, China, in 1995, and the Ph.D. degree in physical geography from Beijing Normal University, Beijing, in 1998.

His research interests include regional net primary productivity estimation, evapotranspiration estimation, and drought monitoring.

Helin Zhang is currently working toward the Ph.D. degree in geographic information system at Beijing Normal University, China.

He is mainly engaged in the research on vegetation productivity product with higher spatial resolution in MuSyQ algorithm.

Zhiqiang Xiao received the Ph.D. degree in geophysical prospecting and information technology from Central South University, Changsha, China, in 2004.

From 2004 to 2006, he was a Postdoctoral Research Associate with Beijing Normal University, Beijing, China. His research interests include the retrieval of land biophysical parameters from remotely sensed data and assimilating radiometric observations into dynamic models.

Anran Zhu received the master's degree in geographic information system from Beijing Normal University, Beijing, China, in 2020.

She is now working in the Xuzhou Economic and Technological Development Zone, Jiangsu Province, China. Her research interests include estimation of light use efficiency of vegetation with remote sensing data.

Mengjia Wang received the master's degree from Beijing Normal University, Beijing, China, in 2018, and she is currently working toward the Ph.D. degree in geographic information system at Beijing Normal University, China.

Her research interests include vegetation productivity and biomass estimation, and vegetation parameter inversion from passive microwave remote sensing data.

Tao Yu received the master's degree from Renmin University of China, Beijing, China, in 2015, and the Ph.D. degree in geographic information system from Beijing Normal University, Beijing, China, in 2019.

His research interests include downscaling of remotely sensed vegetation parameters.

Kunlun Xiang the Ph.D. degree in climate change and environmental ecology from Sun Yat-sen University of China, Guangzhou, China, in 2019.

Since 2019, he has been with the Guangdong Ecological Meteorology Center, Guangzhou, China. His research interests include downscaling of remotely sensed vegetation parameters.